PIXEL-Z: STUDYING SUBSTRUCTURE AND STELLAR POPULATIONS IN GALAXIES OUT TO $Z \sim 3$ USING PIXEL COLORS I. SYSTEMATICS

N. Welikala[1], A.M. Hopkins[2], B.E. Robertson[3], A.J. Connolly[4], L. Tasca[5], A.M. Koekemoer[6], O. Ilbert[5], S. Bardelli[7], J.P. Kneib[5], A.R. Zentner[8]

Draft version December 13, 2011

ABSTRACT

We perform a pixel-by-pixel analysis of 467 galaxies in the GOODS-VIMOS survey to study systematic effects in extracting substructure and properties of stellar populations (age, dust, metallicity and star formation history) from the pixel colors using the pixel-z method. Several systematics are examined in this paper, including the effect of the input stellar population synthesis models whose SEDs are fitted to each pixel's colors, the effect of passband limitations and differences between the individual SED fits to pixels and global SED fitting to a galaxy's colors. We find that with optical-only colors ($bviz$), the systematic uncertainties due to differences among stellar population synthesis codes are well constrained. The largest impact on the stellar population age and SFR e-folding time estimates in the pixels arises from differences between the Maraston (2005) models on one hand and the Bruzual & Charlot (2003) and Charlot &Bruzual (2007) models on the other, when optical-only ($bviz$) colors are used. This results in systematic differences larger than the 2σ uncertainties in over 10 percent of all pixels in the galaxy sample. The effect of varying the number and choice of available passbands is more severe. In 26 percent of the pixels in the full sample, these limitations result in systematic biases in the age determination which are larger than the 2σ uncertainties in the measurements. Robust results can, however, still be obtained with a minimum of 3 optical filters provided they span the 4000 Å break. Near-IR data is also added to a subsample of 46 galaxies from the GOODS-NICMOS survey and systematics arising from model differences are again investigated. Differences among the models in their predicted rest-frame red/NIR colors manifest themselves as follows. For $z > 1$ galaxies the observed optical/NIR colors span the rest frame UV-optical SED, and the use of different population synthesis models does not significantly bias the estimates of the stellar population parameters compared to using optical-only colors. However, for $z < 1$, where the rest-frame NIR is still probed, there is a larger discrepancy between models when using optical-only colors compared to optical/NIR colors. This affects in particular the age determination in the pixels. With this characterization of the systematic errors, we illustrate how pixel-z can be applied robustly to make detailed studies of substructure in high redshift objects such as (a) radial gradients of properties such as age, SFR and dust and (b) the distribution of these properties within subcomponents such as spiral arms and clumps. Finally, we show preliminary results from applying pixel-z to galaxies in the CANDELS survey, illustrating how the new HST/WFC3 data can be exploited to probe substructure and stellar populations in $z \sim 1 - 3$ galaxies.

Subject headings: galaxies: formation — galaxies: evolution — galaxies:statistics

1. INTRODUCTION

1.1. *Clumpy Disks: Resolved Stellar Populations in $z \sim 1 - 3$ Objects as a Probe of High-z Disk Galaxies*

Many galaxies at $z \sim 1 - 3$ have morphologies that are very different from the galaxy population at $z \sim 0$ (Lotz et al. 2004; Lotz et al. 2006; Law et al. 2007; Scarlata et al. 2007; Elmegreen et al. 2007; Pannella et al. 2009). However, the morphologies of these objects only tell one part of the story. At $z > 1$, rest-frame UV wavelengths, which are most impacted by dust obscuration and star formation, can be traced by high resolu-

tion optical imaging (Toft et al. 2007; Overzier et al. 2010; Cameron et al. 2010). The location and distribution of stellar populations within these galaxies, particularly sites of active star formation, is likely to be affected by various physical and dynamical mechanisms which are present in earlier epochs in the galaxy's evolution. The pixel-z technique (Conti et al. 2003; Welikala et al. 2008; Welikala et al. 2009) can measure spatially resolved stellar populations for large samples of $z \sim 1 - 3$ galaxies using their multi-band HST images. With this approach, one can study asymmetries that exist in the star formation, age and dust distribution across these galaxies. In paral-

[1] Insitut d'Astrophysique Spatiale, Bâtiment 121, Université Paris-Sud XI & CNRS, 91405 Orsay Cedex, France, niraj.welikala@ias.u-psud.fr

[2] Australian Astronomical Observatory, PO Box 296, Epping NSW 1710, Australia

[3] Department of Astronomy, University of Arizona, 933 North Cherry Avenue, Tucson, AZ 85721, U.S.A

[4] Department of Astronomy, University of Washington, Box 351580, Seattle, WA 98195, U.S.A

[5] Laboratoire d'Astrophysique de Marseille, CNRS & University Aix-Marseille, 38, rue Frédéric Joliot-Curie, 13388 Marseille Cedex 13, France

[6] Space Telescope Science Insititute, 3700 San Martin Drive, Baltimore, MD 21218, U.S.A

[7] INAF Osservatorio Astronomico di Bologna, Bologna, Italy

[8] Pittsburgh Particle Physics, Astrophyics and Cosmology Center (PITT PACC), Department of Physics and Astronomy, University of Pittsburgh, Pittsburgh, PA 15260, U.S.A

lel with the detailed kinematical studies of these objects from spatially resolved spectroscopy, this will enable insights into the formation mechanisms of these galaxies.

One such mechanism that could be responsible for the formation of these clumps on kiloparsec scales is disk fragmentation in Toomre-unstable gas-rich disks (Elmegreen et al. 2007, Elmegreen et al. 2009). There is now direct kinematic evidence that high-z disks are much more turbulent than their counterparts at $z \sim 0$ (Bournaud et al. 2007; Bournaud et al. 2008; Genzel et al. 2008; Genzel et al. 2011). For example, high-redshift disks have been found to have local intrinsic gas velocity dispersions of $20 - 90 \, \mathrm{km \, s^{-1}}$ as well as high gas-to-total baryonic mass fractions (Daddi et al. 2010; Tacconi et al. 2010). Numerical simulations of gas-rich turbulent disks indicate that massive kpc-sized clumps can form in-situ through gravitational instabilities, a phenomenon known as a 'clump-cluster' phase. (Noguchi et al. 1999; Immeli et al. 2004a,b; Bournaud et al. 2007; Elmegreen et al. 2008; Dekel, Sari, & Ceverino 2009; Agertz et al. 2009; Ceverino et al. 2010; Aumer et al. 2010; Genzel et al. 2010). According to these simulations, the clumps can migrate towards the gravitational center as a result of both their mutual interactions and dynamical friction against the host disk, so that they can eventually coalesce into a young bulge on the order of a few dynamical times.

Alternatively, these high-redshift clumpy disk and irregular galaxies may form via mergers. In particular, numerical simulations of gas-rich mergers result in remnant disks that show a low velocity field asymmetry that also satisfies the criteria necessary to be classified as a high-redshift disk galaxy observationally. For example, Robertson & Bullock (2008) compared one of the merger remnants to the bulk properties of the well-studied $z = 2.38$ galaxy BzK-15504 and showed that it has a star formation rate (SFR), gas surface density, and a circular velocity-to-velocity dispersion ratio that is in excellent agreement with BzK 15504. Such numerical simulations suggest that gas-rich mergers can play a prominent role in the formation of disk galaxies at high redshift.

Recent and upcoming larger IFU programs such as the SINS survey (Förster-Schreiber et al. 2006, Genzel et al. 2006), the SAURON project (Bacon et al. 2001) and the MASSIV survey (Contini et al. 2011; Epinat et al. 2011; Queyrel et al. 2011) are expected to shed further light on these formation mechanisms by performing detailed studies of the gas kinematics of $z \sim 2$ galaxies. Other large IFU programs include the CALIFA project (Sanchez et al. 2011), which will target approximately 600 objects with PMAS IFUs on the Calar Alto Telescope, and the SAMI program (Croom et al. 2011) which is a planned low redshift survey of serveral thousand galaxies. In addition to kinematic studies, a complementary study of the spatial distribution of the stellar populations within these galaxies can provide additional insights into whether these objects are formed through mergers or are, in fact, disks formed in-situ. Förster-Schreiber et al. (2011a, b) used a combination of near-infrared integral field spectroscopy from the SINFONI instrument on the VLT, combined with deep high resolution HST NIC2/F160W imaging of six $z \sim 2$ star-forming galaxies to characterize the properties of kpc-scale clumps and their contribution to the rest-frame op-

tical emission. In our next papers, we aim to extend these previous studies and make detailed spatially-resolved measurements of the properties of large samples of disk galaxies. These studies will also make use of new fully reduced NIR data from the HST Wide Field Camera 3 (WFC3) which will become available for the GOODS-South field in early 2012.

1.2. *Spatially Resolved Star Formation and The Role of Environment in Galaxy Evolution*

The relation between galaxy environment and galaxy properties have been extensively studied in the local Universe (Gomez et al. 2003, Blanton et al. 2005, Hogg et al. 2004). A number of studies have observed that the high-z ($z \gtrsim 1$) SFR-density relation is either reversed or weaker at $z \sim 1$ than that seen locally (Cucciati et al. 2006; Cooper et al. 2007; Elbaz et al. 2007; Ilbert et al. 2006; Poggianti et al. 2006; Ideue et al. 2009; Salimbeni et al. 2009; Scodeggio et al. 2009; Tran et al. 2010; Grützbauch et al. 2011). These examples are consistent with the scenario that galaxies in dense environments form stars rapidly at early times, quickly building up mass and becoming quiescent, while galaxies in less dense environments form stars at a more sedate pace but over longer timescales, a phenomenon we refer to as *in-situ* evolution (Wijeshinge et al. 2011). This is distinct from the infall and quench scenario where the properties of galaxies are impacted directly by their local environment through physical mechanisms such as ram-pressure stripping and galaxy harassment. In addition, Peng at al. (2010) makes a distinction between this type of quenching which is directly related to the environment of galaxies and *mass quenching* which dominates at high masses and early cosmic times.

A few recent studies have, however, continued to observe the same SFR-density relation upto $z \sim 1$ as seen locally (Patel et al. 2011). A few studies have investigated the relation beyond $z \sim 1$. Quadri et al. (2011) showed that galaxies with quenched SF tend to reside in dense environments out to at least $z \sim 1.8$ and that the the SFR-density relation holds even at fixed stellar mass. Their density estimates, however, have relatively high uncertainties as they are derived from photometric redshifts. While the SFR-density relation at high redshifts is a matter of some debate, it is clear that an *in-situ* evolution makes a distinct prediction compared to the infall and quench models. The latter suggests that galaxies in dense environments should show a SFR distribution that is progressively suppressed from the outside in, as the outer regions are those which will be affected first by their rapidly changing environment. The former, on the contrary, suggests that the suppression should either happen uniformly as a galaxy ages, or that the inner regions should be suppressed first. By studying the spatial distribution of SFR in star-forming galaxies as a function of environment, we should be able to distinguish clearly between these two scenarios.

Studies by Welikala et al. (2008; 2009) at $z \sim 0.1$ confirm the global SFR-density relation observed locally but also show that the SFR at $z \sim 0.1$ is centrally concentrated relative to the outskirts, and in more dense environments it is this central SFR that is supressed, favouring the *in-situ* evolution scenario. Park et al. (2007) also studied the color gradients of galaxies as a function of the local galaxy den-

sity and galaxy morphology in the SDSS. They found no environmental dependence of the color gradient for early-type galaxies at a given luminosity, and only a weak dependence on environment for faint late-type galaxies which are observed to become bluer in their outskirts (relative to the galaxy center) in low density environments. It thus becomes extremely interesting to determine whether the radial variation of star formation with environment seen locally is also in place at high redshifts. The development of MOS IFU instruments and surveys with large photometric and spectroscopic samples, such as the Galaxy And Mass Assembly (GAMA) survey (Driver et al. 2011), will allow such a statistical analysis for a large sample of galaxies. There are two complementary approaches to this. While spatially resolved spectroscopy provides detailed measures of the current spatial distribution of physical properties within galaxies, pixel-z adds the ability for the star formation history to be probed. While pixel-z also provides the current SFR and other properties of the stellar populations in subcomponents of galaxies, these measurements will have higher uncertainties than spectroscopic measures, and cannot provide detailed kinematic information that spectroscopic observations can. However, until the advent of highly-multiplexed MOS IFUs, even IFU surveys will be limited to several thousands of targets, while pixel-z can be applied to tens of thousands and up to millions of objects in order to determine the radial variation of stellar population parameters within them and the evolution of this radial variation with redshift. We therefore aim to extend studies performed by Welikala et al. (2008; 2009) which applied the pixel-z method to $\sim 300,000$ galaxies at $z \sim 0.1$ in the SDSS and determined the radial variation of star formation for this sample, the scatter in this relation, and its dependence on galaxy environment and galaxy morphology. There are, however, inherent systematic effects that may limit the utlity of pixel-z in probing spatially resolved stellar populations in galaxies. The current analysis explores these in order to quantify the impact of such systematics on the measurements made by pixel-z.

1.3. *Stellar Populations Extracted from Pixel Colors: Assumptions and Limitations*

A number of studies have sought to extract stellar populations for spatially resolved colors. These compare the colors in individual pixels to a library of SEDs generated by stellar population synthesis models. The majority of these utilised small samples of galaxies at $z \sim 0$ and $z \sim 1$ (Abraham et al. 1999; Johnston et al. 2005; Kassin et al. 2003; Lanyon-Foster et al. 2007; Zibetti et al. 2011). Given a multi-band image of a galaxy, the pixel-z method (Conti et al. 2003; Welikala et al. 2008, 2009) computes the stellar population properties such as stellar population age, SFR e-folding timescale τ, dust obscuration through $E(B-V)$ and metallicity Z in each pixel in the galaxy, as well as the associated uncertainties in these parameters. It does this by taking a library of SEDs generated from stellar population synthesis (SPS) codes, redshifting each of these SEDs and convolving them with the available passbands. The simulated fluxes are then compared to the observed fluxes in each pixel and a best-fitting SED is computed for that pixel. The statistical errors in each parameter are calculated by marginalizing the likelihood

function from the fit over the remaining parameters, and are conservative.

The pixel-z approach makes two fundamental assumptions:

- **Independently evolving pixels:** The pixels in the galaxy image are assumed to be evolving independently of each other. This ignores any mixing of stellar populations between neighboring pixels which is expected to occur in real galaxies. Neighbouring pixels will also not truly be independent, due to a finite Point Spread Function (PSF), and this effect is also neglected.

- **Single stellar populations with exponentially declinining SFH:** The stellar population underlying each pixel is assumed to be one whose spectrum is derived from integrating over single stellar populations (SSPs) of a given age, weighted by a SFR which is characterized by an initial burst followed by an exponential decrease in SFR. The decrease is parameterized by a range of allowed values of e-folding times τ. In reality, galaxies are expected to have more complicated SFHs, including multiple bursts.

In addition to these two fundamental assumptions, there is a limitation in the form of degeneracies among the SED models which could impact the accuracy with which pixel-z determines stellar population parameters in the pixels. SPS models show that age, metallicity and dust all tend to affect spectra in similar ways (Bruzual & Charlot 2003). Multiple SEDs each generated for different populations (different ages, metallicites and SFHs) can, as a result, still predict very similar colors of a galaxy or its subcomponents. Some of these degeneracies arise from well known physical correlations, such as those between age and metallicity of the stellar population. Worthey (1994) constructed detailed models of old and intermediate stellar populations and their absorption indices to show that if $\delta_{age}/\delta Z \approx 3/2$ for two populations, they would appear identical in most absorption indices. The age-metallicity degeneracy can also affect the photometric evolution of the SSPs since optical and near-infrared (NIR) colors reflect the relative contribution of hot and cool stars to the integrated light. Bruzual & Charlot (2003) followed the evolution of optical and NIR colors and the stellar mass-to-light ratio M/L in their model, and found that at fixed age, increasing metallicity tends to redden the colors and increase the M/L ratio. This is explained by the fact that increasing the metallicity (at fixed stellar mass) causes (a) stars to evolve at lower effective temperatures and lower luminosities (Girardi et al. 2000) and (b) changes the relative number of red and blue supergiants, which strongly impacts the color evolution of the SSP. They also found that increasing metallicity at fixed age had a similar effect to increasing age at fixed metallicity. The age-metallicity degeneracy is therefore inherent in the SSP model used. There could also be other degeneracies, including those between dust obscuration and metallicity as well as between age and dust obscuration. The redshift-evolution of the obscuration-metallicity degeneracy in the pixels was characterized by Conti et al. 2003.

This work does not test the two fundamental assumptions above. As for degeneracies, exploring the different correlations between the parameters on a pixel-to-pixel basis and propagating the resulting errors are beyond the scope of this paper. Welikala et al. 2008 characterized some of these correlations using the likelihood function from the fit to the pixels in SDSS galaxies. Since the severity of the degeneracies depend on the number and type of available broadband colors, the SPS model and the chosen grid of stellar population parameters, we focus on these systematics in this paper. The validity of both the two assumptions and the impact of degeneracies will be explored in a future paper that compares the spatial distribution of stellar populations inferred from spatially resolved spectroscopy obtained from large IFU programs (Croom et al. 2011) with those inferred from applying the pixel-z technique to the same galaxies. Such a detailed comparison with IFU programs will enable a robust calibration and testing of pixel-z, leading eventually to a possible refinement of these assumptions. In this paper, we focus on the following systematics that could potentially bias our results:

- **The SPS model:** An inevitable bias is the choice of the stellar population synthesis model. Different stellar population synthesis models predict different colors. In particular, there are significant differences in the prescriptions for Thermally Pulsating Asymptotic Giant (TP-AGB) stars among the following models: Maraston 2005 (M05), Bruzual & Charlot 2003 (BC03) and Charlot & Bruzual 2007 (CB07). In this paper, we compare the outcomes of using these different models on a pixel-by-pixel basis, for all galaxies in the sample. Similar comparisons of population synthesis models have been performed previously on the integrated colors of galaxies but these have focused primarily on the effect on their stellar mass (Maraston et al. 2006). In this work, we focus on the effect of these differences on the age, SFR e-folding time and obscuration estimated in the pixels.

- **The available passbands:** The accuracy with which the pixel-z parameters are determined in the pixels depends on the the available passbands. This paper explores the systematic effects arising from passband limitations, using both optical and near-IR colors.

- **The parameter space searched by pixel-z and the number of SEDs per model:** Pixel-z searches a grid of ages, e-folding times, dust attenuation values and metallicities. In general, a large as possible range of values is chosen while physically unmeaningful values will be associated with high statistical uncertainties. Despite this, a large parameter space can result in degeneracies among the various SEDs searched by pixel-z which in turn may bias the pixel-z estimates. Some priors are already built in to stop pixel-z searching unphysical parameters e.g., the age of a stellar population in a pixel

cannot exceed the age of the Universe at a given redshift. Here, we explore the systematic error arising from increasing the range of parameter values allowed on the pixel-z grid. In particular, we focus on the impact of increasing the metallicity range. This has two predicted effects: (a) it increases the severity of the age-metallicity degeneracy and would bias the pixel-z estimates in quantities such as age, τ and dust and (b) it introduces an uncertainty associated with the models: while spectral synthesis models have been well established for solar metallicity stellar populations in optical photometry, the models are less well established for very sub-solar or super-solar populations. Increasing the metallicity range will test the impact of both these effects on the derived pixel-z parameters.

- **Global SED-fitting versus pixel-z:** We examine any biases resulting from measuring stellar population quantities, particularly the SFR, in individual pixels compared to the same quantities derived from aperture photometry and SED-fitting. These biases arise because individual pixels can have different colors to the integrated color of the galaxy. This bias could give rise to a difference between (1) the mean properties of the galaxy obtained by integrating the fluxes in an aperture and SED-fitting to the total fluxes and (2) the mean properties derived from fitting to the individual pixels within the same aperture and summing the resulting fits.

2. DATA AND METHODS

We use a magnitude-limited ($R < 25$) sample of galaxies in the GOODS-South survey (Giavalisco et al. 2004) with imaging in four ACS bandpasses, $B435$, $V606$, $i775$ and $z850$. We refer to the full set of these four ACS filters as $bviz$ throughout this paper. We make use of the version 2.0 of the publicly available ACS source catalog [9] as well as a photometric redshift galaxy catalog for CDFS (Cardamone et al. 2010). Cutout images of each objects are obtained from the reduced, calibrated, stacked and mosaiced ACS images[10]. The pixel scale in these final drizzled images is $0.03''$.

In the pixel-z analysis, the redshift in each pixel is fixed to that of the host galaxy and we fit only to the SED type. Using spectroscopic redshifts provides a more accurate determination of the stellar population properties in each pixel, compared to using photometric redshifts. We thus select only galaxies which have been spectroscopically measured in the GOODS-VIMOS campaign (Popesso et al. 2009; Balestra et al. 2010). GOODS-VIMOS consists of two surveys which target galaxies in different redshift ranges. The VIMOS Low Resolution Blue (LR-Blue) is aimed at observing galaxies mainly at $1.8 < z < 3.5$ while the Medium Resolution (MR) orange grism is aimed mostly at galaxies at $z < 1$ and Lyman Break Galaxies (LBGs) at $z > 3.5$. Our sample has measured spectroscopic redshifts from both grisms.

A final selection is done on galaxy size to ensure that there are a sufficient number of pixels for the pixel-z

analysis. Galaxies are chosen to have a half light radius $R_{50} > 0.3''$ according to simulations in Welikala et al. (2011) that estimate the minimum galaxy sizes needed to recover color gradients within galaxies with a fractional error smaller than 0.1. This implies that the half light diameter should be at least 20 pixels across, corresponding to 5.5 times the PSF FWHM. This leaves us with a sample of 467 galaxies with four-band imaging ($bviz$). Out of this sample, we select a subsample of 46 objects with NIR colors which have been detected by the GOODS-NICMOS survey (Bouwens et al. 2011; Magee et al 2007; Conselice et al. 2011). This provides deep (> 26.5 mag at 5σ) NICMOS data with the NIC3 camera over the GOODS North and South fields. These studies have found several 'first-light' ($z \sim 7$) galaxy candidates but the survey has also detected several $z \sim 1-3$ galaxies that we use in this work.

The redshift distribution of both the optical and the NIR sample is shown in Figure 1. The median redshift of the optical sample is $z = 0.95$, while that of the NIR sample is $z = 0.81$. For the optical-only sample, there are 145 galaxies in $1.0 < z \leq 2.0$ and 77 galaxies in $2.0 < z \leq 3.0$. For the NIR sample, there are 22 galaxies in $0.5 < z \leq 1.0$, 12 galaxies in $1.0 < z \leq 2.0$ and one object found at $z \sim 3$. Using the Sersic indices (n_{Sersic}) for these objects obtained from a publicly available morphology catalog for the GOODS-South field[11], we find that the optical-only sample consists of approximately 4 times more late-type galaxies compared to early-types: 299 late-type galaxies ($n_{Sersic} < 1.5$) and 81 early-type galaxies ($n_{Sersic} > 2.5$). This study is not concerned with tracing a particular population of galaxies, which would require a volume-limited sample of objects. Rather, we investigate systematics of a particular technique which can be applied to galaxies in a range of redshifts, luminosities, morphological types and inclinations as long as they are well-enough resolved for the pixel-z analysis. Nevertheless, we repeat our analysis on subsets of the full galaxy sample in order to test the robustness of the results against selection effects.

Finally, we use preliminary NIR data from the first 6 epochs of the CANDELS survey (Grogin et al. 2011; Koekemoer et al. 2011) using the WFC3 $F125W$ and $F160W$ filters in the GOODS-South field[12], in order to illustrate the power of combining this high resolution optical and NIR data from ACS and WFC3 with the pixel-z method in order to probe substructure in $z \sim 1-3$ galaxies and to determine the properties of the stellar populations in the pixels. A more thorough investigation of substructure in galaxies using the final CANDELS data product will be performed in a future paper.

2.1. Obtaining Fluxes and Variances in the Pixels

ACS and NICMOS science images are in counts/sec, while the weight maps are inverse variance maps (i.e., $1/\sigma_f^2$). Flux calibration of the ACS and NICMOS science and weight postage stamp images of each source is peformed using the ACS[13] and NICMOS zeropoints[14]. These contain the background variance from the sky noise, readout noise and dark currents.

Further, because the pixels are correlated, the actual noise is higher than the theoretical noise in the weight files (Casertano et al. 2000). We account for this by computing the noise in empty patches (whose size is larger than the correlation length scale) within the science image and we calculate the ratio of this measured noise value to the theoretical noise value. The noise in the weight images is then rescaled by this ratio to give a more accurate estimate of the noise in the pixels due the background and instrument. The Poisson uncertainty from pixels in the source itself is then added in quadrature.

These final ACS flux and variance images are resampled to the coarser 0.1 arcsecond pixel scale of the NIC3 images using a Lanczos4 kernel. We then perform PSF-matching of the ACS images to the NIC3 images using the *ip_diffim*[15] image mapping software currently in the pipeline of the Large Synoptic Survey Telescope (LSST). The *ip_diffim* code is an implementation of the Higher Order Tranform of Psf and Template Subtraction code (*Hotpants*[16]), and uses the algorithm of Alard (1999) and Alard & Lupton (1998) to find the PSF-matching kernel that maps the input (resampled) ACS images to the NIC3 ones. The kernel is decomposed into a linear set of basis functions, which are Gaussians of varying FWHM. The process is linear and ends up matching the PSFs of the two input images. A similar process is used to PSF-match the variance images. Finally, for the analysis on the CANDELS data, the WFC3 images from the first 6 HST epochs are stacked by performing a weighted sum of the images in the different epochs and dividing by the sum of the weight maps[17] in order to increase the signal-to-noise in the final flux images. The existing ACS images are resampled to the pixel scale of the WFC3 ones and PSF-matching is performed using the same method.

2.2. Deriving SSPs from Colors with pixel-z

The pixel-z method (Conti et al. 2003; Welikala et al. 2008; Welikala et al. 2009) fits SEDs from a library of stellar population synthesis models to colors of individual pixels. The redshift is fixed to the spectroscopic redshift of the galaxy, and the fitting is done for the SED only. A best-fitting SED is identified for each pixel using a maximum likelihood method and an age, τ, dust obscuration and metallicity is then inferred for each pixel. RMS errors are found for each of these parameters by marginalizing the likelihood function in each pixel over the remaining parameters. A signal-to-noise threshold $SNR > 5$ in the i band is set to ensure that the fitting is done to pixels in the galaxy and not to the sky pixels. Low SNR pixels in the outskirts of a galaxy and in any residual sky pixels that have been artificially fitted generally have the largest

uncertainties in their pixel-z parameters.

We examine three distinct stellar population synthesis models which are currently widely used: Bruzual & Charlot 2003 (BC03), Charlot & Bruzual (CB07) and Maraston 2005 (M05). For each model, we generate spectra derived from single stellar populations with an exponentially declining star formation history. In order to test differences between the codes, the parameter space has to be made identical (or if not, as similar as possible). The grid of stellar population parameters ecompasses 2178 SEDs:

- 11 values of stellar population age: this is the time elapsed since the intial burst of stars. The stellar populations range from extremely young (0.001, 0.01, 0.1, 0.5 Gyr), to middle age (1.0, 3.0, 5.0 Gyr) to very old (7.0, 9.0, 11.0, 12.0 Gyr). In addition, the pixel-z algorithm rejects ages which are greater than the age of the Universe at the redshift of each galaxy.

- 11 values of τ: 0.1, 0.25, 0.50, 0.75, 1.0, 1.5, 2.0, 3.0, 4.0, 5.0, 10.0 Gyr.

- 6 values of $E(B - V)$ from the Calzetti al. 1998 attenuation curves: 0.0, 0.1, 0.2, 0.3, 0.5, 0.9.

- 3 values of metallicity Z: 0.01 (0.5 $Z_\odot$) and 0.04 (2 $Z_\odot$).

In the case of metallicity, stellar populations generated from the M05 models allow only 3 values. We have adopted 3 values of Z across all the models compared here (in BC03 and CB07, these are 0.008, 0.02 and 0.05). To test the effect of this restricted metallicity range, we perform a control test over the entire population of galaxies and all the associated pixels, using the BC03 models. The allowed number of metallicities is increased to include significantly sub-solar values ($Z = 0.0001, 0.0004, 0.004$). The resulting systematic error, i.e., the difference in each pixel-z parameter (age, τ, $E(B - V)$) between using 6 values and 3 values of Z, is computed pixel-by-pixel, and we examine the distribution of this systematic acrosss the entire galaxy sample. The effect of this relatively restricted range of metallicity is that the systematic difference in the Z values recovered from pixel-z between the models is usually no more than 1 σ, indicating that the majority of pixels in the galaxy sample are described by metallicites which are close to solar. Permitting only metallicities that are close to solar is therefore a reasonable approximation. The effect on the other parameters (age, τ and dust obscuration) is examined below. This control test is also a test of the impact of degeneracies in the models used. Increasing the input metallicity range would be expected to increase the severity of these degeneracies when fitting to the pixel colors, and therefore increase the systematic error in the pixel-z parameters. The results of this test are presented in section 3.2.

2.3. Measuring the Systematic Effects

2.3.1. Measuring systematic effects in pixels for all galaxies in the sample

In the tests below, we compute the ratio of the systematic error in a particular pixel-z quantity (age, τ,

$E(B - V)$) to the statistical error in that quantity, for each pixel in the galaxy:

- When testing the effect of the stellar population synthesis models, we measure for each pixel and for each parameter q the quantity f, where:

$$f(m1, m2) = \frac{q(m1) - q(m2)}{\sqrt{\sigma_q(m1)^2 + \sigma_q(m2)^2}} \qquad (1)$$

where $m1$ and $m2$ are the 2 models being compared and σ_q is the rms uncertainty in the parameter q for that pixel.

- When testing the effect of limiting the available passbands, we measure for each pixel and for each parameter q the quantity

$$f(p1, p2) = \frac{q(p1) - q(p2)}{\sqrt{\sigma_q(p1)^2 + \sigma_q(p2)^2}} \qquad (2)$$

where $p1$ and $p2$ are the filter set used.

- The systematic error resulting from expanding the metallicity range from 3 to 6 values is computed similarly.

For each galaxy in the sample, we measure f within $2R_{50}$, considering only pixels with $S/N > 5.0$ to remove sky pixels. Since the effect of each systematic could vary from galaxy to galaxy, we are interested in the distribution of a particular systematic error across the whole galaxy sample. For each test of a particular systematic, we plot the distribution of f for all the pixels inside $2R_{50}$ for all the galaxies in the sample. With such statistics, we are able to determine conclusively the effect of the particular systematic being tested. We check how robust the results are against selection effects by repeating the analysis on several independent subsets of the galaxy sample. In particular, we find that, for the optical-only sample, the results are robust against the effect of redshift. We thus present our results for the full sample for the optical-only case. When considering only the 46 galaxies of the NIR sample and comparing the results of using only the optical data for this sample with those obtained using the optical and NIR data combined, we find a small difference in the results for galaxies with $z < 1$ and $z > 1$. For the NIC3/NIR sample, therefore, we present our results for $z < 1$ and $z > 1$ separately.

2.3.2. Estimating the bias from using pixel-z relative to global SED fitting

We estimate the bias in the inferred stellar population parameters from using pixel-z relative to the global quantities inferred from aperture photometry. In particular, we investigate whether the sum of the SED fits to individual pixels in a galaxy is consistent with the fit to the total flux from the same pixels. These differences can arise because individual pixels can have colors that differ from the mean color of the galaxy. As a result, individual pixels can have stellar population quantities that can differ significantly from what is derived from the integrated colors of galaxies. The result of summing the fits to the individual pixels in a galaxy may, in principle, be significantly different from the global quantity measured from SED-fitting to the total

fluxes of the same pixels. Our aim is to investigate these differences and quantify their magnitude.

We focus on the SFR since it is a direct observable in spectroscopic (including spatially resolved spectroscopic) measurements. In both approaches, the current SFR is derived using the best-fit star formation history, normalized using the same scale factor required to normalize the SED to match the observed broad-band luminosity, in either the pixel (for the first approach) or the entire galaxy (for the second). We perform the comparison of the two approaches for the same pixels by considering only pixels with $S/N > 5$ and within a fixed aperture of radius $0.5''$. We use the same library of SED templates throughout the comparison: 2178 SEDs generated by the BC03 models. The residual difference between the sum of the SED fits to the invidual pixels and the SFR derived from SED-fitting to the total flux in the same pixels is then computed in terms of the statistical error in the SFR measurement.

2.3.3. *Substructure measurements: radial stellar population gradients, spiral arms and clumps*

As described in Section 1, we aim to use pixel-z to study (a) the spatial distribution of SFR and dust and its dependence on the galaxy environment and (b) clumpy star-forming disk galaxies at $z \sim 2$. We use selected face-on disk galaxies to demonstrate how pixel-z can be used to measure large-scale features such as radial stellar population gradients and to compute the mean properties of spiral arm structures and clumps. We also wish to know how the different systematic errors computed for the individual pixels, as described in section 2.3.1, translate to systematics in these large-scale features in the galaxy.

- **Radial gradients of stellar populations:** We compute the mean luminosity-weighted age, τ and E(B-V) of successive radial annuli in the galaxy. The luminosity L_i in each pixel is computed directly from the normalization of the best-fitting SED template to the observed fluxes. The mean pixel-z quantity $\langle q_j \rangle$ computed in annulus j is thus:

$$\langle q_j \rangle = \frac{\sum_{i=0}^{N} q_i \times L_i}{\sum_{i=0}^{N} L_i} \quad (3)$$

where N is the number of pixels in the annulus.

From the age, τ and L in each pixel, two futher quanties, the $\langle SFR \rangle$ and the mean specific star formation rate ($\langle sSFR \rangle$) are also derived for each annulus. The gradients of these quantities are then computed for (a) varying stellar population synthesis models and (b) varying passbands. The size of the smallest annulus is chosen such that it is larger than the full width half maximum (FWHM) of the PSF in the i band. The radius in *kpc* is computed directly from the spectroscopic redshift of each galaxy and the ACS angular scale of $0.03''$/pixel, and assuming $\Omega_\Lambda = 0.728$, $\Omega_M = 0.27$, and $H_0 = 70.2 \, \mathrm{km \, s^{-1} \, Mpc^{-1}}$.

- **Mean properties of spiral arms and clumps:** We use the GALFIT code (Peng et al. 2002; 2010) to isolate components such as spiral arms and

clumps for selected face-on disk galaxies in our sample. A disk galaxy model is subtracted from the galaxy image in the i band and the residual image is then used as a mask to effectively isolate both the spiral arms and clumps in the galaxies. These structures of interest correspond to the tail of the flux distribution in the residual image, and by adjusting the threshold, we are able to isolate the components individually. The pixel-z code is then run on the total fluxes of the pixels identified as being part of these substructures. The distribution of the age, τ, $E(B-V)$, SFR and sSFR of all the pixels belonging to each clump/spiral arm is then calculated for the different cases of stellar population synthesis models.

We perform these analyses on selected disk galaxies, an example of which is shown in this work, in order to identify preliminary trends, and to refine our approach for a more thorough investigation. A statistical study of radial gradients, spiral arms and clumps, which will also require a more careful selection of galaxies, will be explored in a future paper.

3. RESULTS AND DISCUSSION

3.1. *Effect of SSP Model Differences using Optical-only Bands*

Here, we illustrate the effect of using different stellar population synthesis models on the values of the parameters that pixel-z determines using the *bviz* passbands. This is first shown qualititatively by displaying the resulting maps, and second, quantitatively, by measuring the systematic error in each parameter and following its distribution.

In the top panel of Figure 2, we illustrate the effect of the chosen stellar populations model on the age maps. There is a clear correlation between the pixel-z maps of this galaxy and the i band image. The qualitative differences from pixel-to-pixel between the various models(M05,BC03,CB07) are small but there is a difference along the right spiral arm between BC03 and CB07 on the one hand and M05 on the other. BC03 and CB07 both predict that the majority of pixels along the arm have ages ~ 0.1Gyr, while M05 shows a larger proportion of pixels showing younger ages (~ 0.01Gyr). Otherwise, both age values and their associated uncertainties in the pixels are qualitatively similar for all 3 models. The red pixels in the inter-arm regions indicate much older populations but since these are also typically lower signal-to-noise pixels, the rms error is also significantly worse for these pixels. Pixels belonging to the sky which are artificially fit are also assigned large uncertainties.

The dust obscuration, shown in Figure 3 is also correlated with the spatial distribution of the stellar age. Unlike the disagreement seen in the age values of the spiral arm between the M05 models on one hand and the BC03 and CB07 models on the other hand, the obscuration maps demonstrate a high level of agreement among the various models. In all the models, the arm regions, which were predicted to have the youngest stellar populations, also have a moderately high level of dust obscuration, with $E(B-V) \sim 0.5$. The uncertainties in the dust obscura-

tion in the pixels are similar among the various models as well. These uncertainties correlate strongly with morphological features in the image as in the case of the stellar population age. The knots on the spiral arms, corresponding to star-forming HII regions, are clearly displayed in the obscuration uncertainty map with the lowest errors of the entire galaxy. These statistical uncertainties are similar among all the models considered. The inner arms and the outermost edges of the galaxy, which are the regions with the lowest signal-to-noise in the entire galaxy, have, predictably, the highest rms uncertainties in their pixel-z quantities.

In order to quantify these effects, we use pixels from all 467 galaxies in our sample. The systematic error due to different population synthesis models is measured according to equation 1, with the resulting distribution shown in Figure 4. The distributions are generally non-Gaussian, peaking around zero systematic error, and showing a relatively small fraction of outliers. The shape of the distribution is a result of the quantized nature of the problem, since the pixel-z parameters lie on a discrete grid of values. The level of agreement and the fraction of outliers in this distribution for every pixel-z parameter is summarized in Table 1 for each of the pairs of models being compared. The two models that have the highest level of agreement in all the parameters concerned (age, τ and E(B-V)) are BC03 and CB07. In the τ parameter, 94 percent of pixels within the galaxies are within 1σ and the fraction of outliers ($> 2\sigma$) is 0.04. The high level of agreement between BC03 and CB07 is due to the fact that the continuum in the rest-frame UV is very similar between these two models. There is a larger systematic difference in the pixel-z parameters between BC03 and M05, and between CB07 and M05. In particular, the τ parameter is most sensitive to differences between these models. The fraction of pixels with a systematic difference in τ less than 1σ, is 0.71 and 0.80 for the [BC03,M05] and [CB07,M05] model pairs respectively. The fraction of outliers in τ ($> 2\sigma$) is 0.15 and 0.17 respectively for the same model pairs.

The impact of model differences between BC03/CB07 and M05 is much smaller for the age and obscuration. Dust obscuration is least sensitive to differences between any of the 3 models, with only $1 - 3$ percent of pixels having systematic differences in $E(B - V)$ which are larger than 2σ. For the inferred stellar age, the fraction of pixels having systematic differences in their stellar population age of $< 1\sigma$ is 0.86 and 0.87 for [BC03,M05] and [CB07,M05] respectively, while the fraction of outlier pixels in the age distribution for the same pairs of models is 0.11. For [BC03,CB07], 0.94 of pixels agree in their inferred stellar population age to within 1σ, while the fraction of outlier pixels for the same models is 0.04. The comparison of the stellar population synthesis models for the metallicity are not shown in Table 1 because the small number of values of metallicity being sampled means that all fits are within 2σ.

Out of the three pixel-z parameters tested, it is thus in the SFR e-folding time where the largest discrepancy lies between M05 on one hand and BC03/CB07 on the other. This discrepancy is unlikely to be due only to the differing treatment of TP-AGBs stars in these models, since if that were the case, we would expect better agreement between CB07 and M05 as contrasted against BC03. The discrepancy observed in τ is likely related to fundamental differences between M05 on one hand and BC03/CB07 on the other when the SED fitting is performed using optical colors only. In section 3.5.2, we use some example galaxies to investigate where the discrepancy in the predicted values of τ (between M05 and BC03/CB07) occurs spatially in the galaxies. Finally, we test the effect of redshift on these results by repeating the above analysis for subsamples of galaxies in redshift intervals of 0.5 from $z = 0.5 - 3$ and find that our results for the optical-only passbands are not significantly impacted by the redshift of the galaxy.

3.2. *Effect of Parameter Space and SED Degeneracies*

In this test, we examine the effect of changing the parameter space on the pixel-z estimates using the BC03 models. The number of metallicity values used in the pixel-z grid of stellar population parameters is increased from 3 to 6, to include sub-solar metallicities, as detailed in Section 2.2. The increase in the metallicity range means we are comparing the original 2178 SEDs with an expanded set of 4356 SEDs fitted to each pixel.

The distribution of the systematic error (as a function of the statistical error) introduced by extending the allowed metallicity range into the sub-solar regime is shown in Figure 5 for all pixels in all the galaxies in the sample. The fraction of pixels with small systematic errors ($< 1\sigma$) and the fraction of outliers in each parameter is summarized in Table 2. The largest effect of a broadening the metallicity range is, predictably, on the stellar population age but the effect is minimal: the fraction of outliers in the age systematic is only 0.06. Around 6 percent of pixels have a bias in their τ that is larger than the 2σ uncertainties. The obscuration is the parameter which is least affected (< 0.01 of pixels) by the introduction of sub-solar metallicities. This is in agreement with the findings of Conti et al. (2003) who examined the evolution of the obscuration-metallicity degeneracy in pixels in galaxies in the HDF-North, and found that there is a strong degeneracy in galaxies at low redshifts but that the relation flattens out at $z > 1$.

The conclusion of this test is that while the stellar population age and τ are marginally affected by the increased metallicity range, as expected from the age-metallicity degeneracy, the resulting systematic differences in all the pixel-z quantities are still well within the uncertainties between different stellar population synthesis models.

3.3. *Effect of Passband Limitations (Optical-only)*

Here we test the effect of the passband limitations on the estimates of the pixel-z parameters. The stellar population synthesis model is fixed to BC03 in this test and passbands are added and removed and the pixel-z output is compared to that produced using the full complement of 4 optical bands. This test is initially performed for selected individual galaxies to identify the likely trends, before a full investigation on all pixels in the full galaxy sample is performed. Figure 6 illustrates the test for one example galaxy, which is the same as shown in Figures 2 and 3. It shows the impact of passband variations on the age values in the pixels and their associated uncertainties. Starting with only 2 optical bands (bv), the effect of different permutations of bands are tested. From the stellar

population age maps, it is clear that 2 passbands are insufficient to resolve many of the features seen in the light distribution of the galaxy. For the case of 3 bands, the use of the redder viz combination of filters comes closer to the result obtained with the full $bviz$ filters than does the bvi set. The viz combination produces an age map that comes closer to mirroring the galaxy morphology than does the bvi set, separating the arm and inter-arm regions more clearly. For this example galaxy at $z \sim 1$, most of the relevant color information for the pixel-z therefore comes from the optically redder passbands.

A similar conclusion can be drawn from the map of rms values in the age parameter. With only 2 optical bands, high uncertainties throughout the disk of the galaxy reflect the inability of pixel-z to find the correct SED with only 1 color, thus resulting in higher statistical errors in the ages inferred for the pixels. With 3 passbands, again it is the viz combination that seems to be closest to the $bviz$ values. However, the maps of dust obscuration in Figure 7 show that the bvi combination coming closest to the result predicted from the full complement of bands. Nevertheless, the bvi, viz and $bviz$ combinations all agree that the arms have intermediate levels of obscuration ($E(B-V) \sim 0.4$) and low associated RMS errors.

Moving to the full sample of all pixels in all galaxies, we use equation 2 to compute for each parameter and for each pixel, the systematic error (again in terms of the statistical error in the parameter) due to the difference between a given filter permutation and the full optical filter set ($bviz$). The stellar population model is fixed to BC03 as before. Figure 8 shows the distribution of this systematic error for all the pixels in the full galaxy sample. It is evident that the systematic error distribution has larger tails and a lower peak ($< 1\sigma$) than the systematic errors resulting from stellar population model differences. As for the example galaxy in Figures 6, it is clear also that 2 filters (bv) result in a large fraction of outliers ($> 3\sigma$). For the 3-filter permutations (biz, bvi and viz), across the entire sample of galaxies, we find that there is only a small difference in the distribution of the systematic error among the filter permutations.

We show the fraction of outliers in each case in Table 3. It is clear that the SFR e-folding time (τ) and the stellar population age are the most impacted of the 3 parameters by passband limitations. In τ and in the stellar population age, over 20 percent of the pixels become outliers ($> 2\sigma$) when one band of the full filter set $bviz$ is dropped. There is not a very significant difference between the 3 sets of filters, but omitting the z band results in an outlier fraction for the τ parameter of 0.26 compared to 0.20 for the other bands. For the stellar population age, the outlier fraction varies from $0.22-0.28$ relative to the full filter set ($bviz$). The dust obscuration is least impacted by passband changes, as long as a minimum of 3 are used. For each of the 3 filter sets, about 80 percent of pixels in the full galaxy sample have an $E(B-V)$ which agrees with the $bviz$ result to within 1σ. Finally, as in Section 3.1, we test the effect of redshift on these results by repeating the above analysis for subsamples of galaxies in different redshift intervals from $z = 0.5-3$ and find that our results for the optical-only passbands are not significantly impacted by the redshift of the galaxy.

3.4. *Effect of Adding the Near-IR Data*

In this section, we explore the effect of adding NIR passbands from NIC3 to the existing optical data for a subsample of 46 galaxies. Adding the NIR data allows us to explore systematic differences between various population synthesis models more fully, since they can predict different NIR colors. In particular, it is known that BC03 and M05 differ significantly in their treatment of TP-AGB stars, consequently resulting in different predicted NIR colors. This is illustrated in Figure 9 which shows an example SED from all three models considered in this work, for a galaxy at $z = 1.0$ containing a stellar population that is 3 Gyr old, with $\tau = 10$ Gyr, $E(B-V) = 0.9$ and $Z = 0.008$. There is very little difference between the shape of the continuum between the the models in the optical. However, the same galaxy in the NIR shows significant differences in the shape of the continuum among the three models. These will give rise to different predicted NIR colors in the pixels.

Figures 10 and 11 show examples of applying pixel-z to a galaxy at $z = 2.5$ with $bviz$ and J and H band imaging from NIC3. There is a good agreement among the three models compared here in both their stellar population age maps and in the age rms map. All three models predict a very young population of stars throughout ($t < 0.2$ Gyr). All models considered predict the core of the galaxy to have an older population of stars (~ 0.1 Gyr) than the outskirts ($t \sim 0.01$Gyr). The one notable difference is that the M05 models predict a slightly larger proportion of very young stellar populations ($t \sim 0.001$Gyr) surrounding the nucleus. The models also agree very well on the age distribution within the companions of this galaxy (to the right). The models also agree well in the uncertainty maps in the stellar population age. Figure 11 shows the obscuration maps of the same galaxy as predicted by the three models. Again, there is excellent agreement among the three models in the distribution of dust and its associated uncertainty. In general, all three models predict that the galaxy has moderate levels (E(B-V)~ 0.3 magnitudes) of dust, but they also show pockets of high obscuration (E(B-V)~ 0.5 magnitudes) within the main galaxy and also in its two companions. The location of these pockets are the same in three models. This example therefore implies that model differences do not introduce large systematic biases in the pixel-z parameters for $z \sim 2.5$ galaxies with such irregular morphologies.

We investigate this hypothesis fully when we measure systematic differences across all pixels in the combined optical-NIR galaxy sample for all 3 models considered in this paper. For each parameter, we compare this distribution of the systematic differences with that obtained with using only the optical data. We account for the effect of redshift, particularly because for $z > 1$, the 4000 Å break shifts into the J and H passbands. We thus split the NIR sample into two: $z < 1$ and $z > 1$. In Figure 12, we show the distribution of the systematic difference between models for the low redshift sample. The fraction of pixels showing $< 1\sigma$ uncertainties in their pixel-z parameters for each pair of models is given in Table 4 for both the optical-only colors and the optical and NIR colors. For the low redshift sample, there is a very high level of agreement between the BC03 and CB07 models in all the pixel-z pa-

rameters, with over 97 percent of pixels showing less than 1σ deviation between the two models. With the addition of the NIR bands however, the systematic differences between BC03 and CB07 models are exposed. This is a result of relatively small differences among the models in their predicted rest-frame UV colors but much larger differences among them in their predicted rest-frame optical (red) and rest-frame NIR colors. This affects in particular the stellar population age (with only 78 percent of pixels showing less than 1σ difference between the two models) and τ (88 percent of pixels showing agreement between the two models). The obscuration is less impacted by the model differences. The addition of the NIR colors also exposes differences between BC03 and M05, and this impacts the stellar population age most strongly, with the fraction of pixels showing $< 1\sigma$ difference in the age decreasing from 0.89 with optical-only colors to 0.80 with NIR colors. The differences between BC03 and M05 have less impact on τ and the obscuration when the NIR colors are added. When comparing CB07 with M05, it is again the stellar population age in the pixels that is most affected by the addition of the NIR passbands, with only 80 percent of pixels showing an agreement in the age to within 1σ between the two models, compared to 89 percent for the optical-only case.

For the high-redshift ($z > 1$) sample, the story is somewhat different, as illustrated in Figure 13 and Table 5. There is now a much higher level of agreement between the results for the optical-only colors and the optical and NIR colors combined, for all the parameters concerned. This is due to the fact that the rest-frame UV and blue wavelength optical spectra (which are sampled by the optical and the NIR filters for $z > 1$) are similar among the models. This similarity in the predicted rest-frame UV/optical (blue) colors among the models thus manifests itself as follows. In the $z < 1$ sample discussed above, the stellar population age showed a large discrepancy between the $bviz$ and $bvizJH$ samples in terms of the fraction of pixels that agree on their age for the different models being compared. For the high redshift sample, the pixels in both the $bviz$ and $bvizJH$ samples show similar levels of agreement in the age parameter between the different models compared. For example, for the the BC03 and M05 models, the fraction of pixels with systematic differences in their age that are smaller than 1σ is 0.95 in the optical-only case and 0.93 in the NIR case. The conclusion of these tests is that, for $z > 1$ galaxies, differences among the stellar population synthesis models in their predicted NIR colors do not significantly bias the pixel-z estimates of the stellar population parameters in the pixels, compared to using optical colors only.

3.5. Global Galaxy Properties and the Effect of Systematics

Pixel-z can measure global properties of structures composed of many pixels within the same galaxy. These will be used to determine the radial variation of stellar population parameters in galaxies as a function of the galaxy environment, and also to allow a detailed study of high redshift clumpy, disk galaxies, as outlined in Section 1.1 and 1.2. Here, we investigate the effect of systematic biases that can impact these global measurements, in particular of the SFR since this will be a direct observable in spectroscopic measurements.

3.5.1. Biases from using pixel-z versus global SED-fitting

In Figure 14, we show the level of consistency between the sum of SED fits to individual pixels in a galaxy and the global fit to the total flux in those same pixels, as described in Section 2.3.2. We see a high level of consistency between the two approaches in their estimates of the integrated SFR. We also quantify the magnitude of any deviation between the two approaches in terms of the statistical uncertainty in the SFR estimate for each galaxy from SED-fitting. We see that for the majority of galaxies in the sample, the difference between the two SFR estimates for the galaxies are within the statistical uncertainties of the SFR measurement. However, there is a small population of outliers ($> 2\sigma$) which are galaxies with low SFR ($< 1 M_\odot \, yr^{-1}$) and which show a negative residual i.e., the SFR estimates from pixel-z, obtained by summing the results of the individual fits in each pixel, are higher than the SFR estimates from global fits to the total flux in the pixels. In addition, there is a second small population of outliers which are galaxies with high SFRs ($\sim 10 M_\odot \, yr^{-1}$). In these, the SFR estimate from the global fit is significantly higher than that estimated from the sum of the individual SED fits.

3.5.2. Radial gradients of stellar populations: age, dust and star formation

In Figure 15, we present the radial variation of the stellar population age, SFR e-folding time, obscuration, SFR and sSFR using the $bviz$ passbands for the same galaxy at $z \sim 1$ in Figures 2 and 3. The radial trends in each quantity are measured according to the method described in section 2.3.3. All stellar population synthesis models agree on the qualitative trends of all the parameters with radius but there are some quantitative differences that arise, particularly between the different population synthesis models All three models agree that the stellar populations in the galaxy at all radii are young (< 0.3Gyr) and that the stellar population age decreases rapidly from the center to the outskirts. M05 predicts a mean stellar population age that is somewhat lower in the innermost part of the galaxy compared to BC03 and CB07, and this systematic difference is of the order of the statistical uncertainty in the age measurement. BC03 and CB07 also predict a somewhat sharper drop in the stellar population age between 2 and 3 kpc, but again, the difference is well within the statistical uncertainties.

The models agree on a range of $\tau \sim 0.5 - 1$ Gyr across the galaxy. Between 3 and 5 kpc, however, the M05 model prediction diverges by 1σ from both BC03 and CB07 models. This region corresponds to the spiral arm and the clumps of star-forming HII regions within it. This implies that the different treatment of TP-AGB stars in M05 compared to the other models has its biggest effect in the spiral arms of the galaxy. The dust obscuration trends are quite similar among the models which show that the center of the galaxy is moderately obscured ($E(B - V) \sim 0.45$). The obscuration then decreases up to 2 kpc and then increases to a maximum ($E(B - V) \sim 0.6$) in the spiral arms.

The different models all find that the mean SFR in each annulus peaks in the center of the galaxy. To explain this,

we note that the current SFR is determined not only by the mean age and τ of the stellar populations, but also by the total stellar mass formed to date, which normalizes the SFR. M05 predicts a lower stellar mass throughout the galaxy than does BC03 or CB07. When the stellar mass is normalized out to give the specific SFR (sSFR), we see that the discrepancy between M05 and BC03/CB07 narrows considerably: 1σ at most in all radial bins. Comparing the trend in sSFR with the morphology of the galaxy, we conclude that the bar structure in the center of the galaxy is actively star-forming. The models disagree, however, on how much more star-forming the bar is relative to the spiral arms at a radius of ~ 4kpc. BC03 and CB07 predict a slightly higher sSFR (by around $2 \times 10^{-11} \, yr^{-1}$) in the center of the galaxy compared to the spiral arms, whereas M05 predicts a somewhat lower sSFR in the center relative to the spiral arms. Nonetheless, a general picture emerges for this galaxy, which is that star formation is not simply confined to the center but takes place throughout the galactic disk. The results, albeit for a single galaxy, imply that pixel-z is robust to differences between various stellar population synthesis codes when it is used to measure radial variations across galaxies.

Figure 16 shows the effect of passband limitations on measuring radial variations of stellar population parameters. The population synthesis model was fixed to BC03. Using only the b and v bands results in large systematic uncertainties which affects all the radial quantities but particularly the mean age and the obscuration determinations. The result of using only the b and v bands is that the mean age is overestimated throughout the galaxy relative to the $bviz$ filter set, by as much as 4σ. This can be explained by the fact at $z \sim 1$, the 4000 Å break passes out of the bluest optical bands and, as a result, the colors predicted by the model for the pixels are redder, leading to an older stellar population for the pixels. The obscuration is underestimated throughout, and at a radius of 4 kpc the difference with respect to the $bviz$ value is as much as 4σ. The τ and the sSFR estimates are less impacted by the loss of 2 passbands.

The 3-passband combinations bvi and viz both come closest to reproducing the $bviz$ radial trends in all the parameters. The systematic difference between the bvi and viz combinations is relatively small, but some differences do emerge nevertheless. In the center of the galaxy, the viz filter combination predicts a larger (by 1σ) mean stellar population age than the bluer bvi bands. Elsewhere in the galaxy, the three-filter combinations give results which are consistent (within their statistical uncertainties) with each other and also with the full $bviz$ filter set. The radial variation of the dust obscuration is consistent among the bvi, viz and $bviz$ filter sets except in the innermost annulus where the viz filters underpredict the level of obscuration relative to the other two combinations. The differences in τ are small, although there is one important difference at $r = 3$kpc where the bvi set predicts a higher τ compared to the viz and $bviz$ sets. The effect of filter cominbations on the sSFR is also relatively small throughout the galaxy except in its outermost part ($r \sim 5$kpc) where the three-filter combinations overestimate the sSFR relative to the full optical set.

If we were to generalize this test, a minimum of 3 opti-

cal passbands are therefore needed for robustly computing radial trends of stellar populations in these high redshift galaxies.

3.5.3. Disk galaxies at $z \gtrsim 1$: spiral arms and clumps

In Figures 17, 18 and 19, we illustrate the way pixel-z can be used to study the stellar populations of subcomponents of galaxies such as spiral arms and clumps, and we explore how this can be biased by the choice of the SPS model. The optical filter set $bviz$ is used throughout this analysis. In the spiral arm of the disk galaxy which has been isolated, the BC03 and CB07 models predict almost identical distributions for the parameters among the pixels that make up the spiral arm. In contrast, some differences start to emerge between M05 and the other two models. The age distribution of the pixels peaks at 0.1 Gyr for the BC03 and CB07 models, and at a lower age (0.01 Gyr) for the M05 model. All three models show good agreement for the dust distribution among the pixels in the arm, which peaks at 0.5 Gyr. There is however a systematic offset in the SFR distributions which peak at 0.003 $M_\odot \, yr^{-1}$ with M05, whereas it peaks at 0.03 $M_\odot \, yr^{-1}$ with BC03/CB07. This difference is largely due to the lower stellar mass predicted for the pixels in the arm by M05 compared to the other models. When stellar mass is normalized, we see a much closer agreement between M05 and BC03/CB07. All the models predict a sSFR distribution that is bimodal in the arm, one peaking at $10^{-9.8}yr^{-1}$ and the other at $10^{-8.3}yr^{-1}$.

We also investigate clumps in the disk and the impact of model differences on the inferred properties of clumps in the disk of the galaxy. Clump A in Figure 18 is part of the outer arm of the galaxy. As in the case of the spiral arm, the distribution of the stellar population age and dust obscuration among the pixels in clump A, is quite similar among the different population synthesis models. As with the full spiral arm, a substantial difference exists in the SFR distributions. The M05 models predict the clump to have a lower SFR than BC03/CB07. The distribution peaks at $\sim 0.01 M_\odot \, yr^{-1}$ with M05 and $0.3 M_\odot \, yr^{-1}$ with BC03/CB07, due to a lower stellar mass predicted for the clump by the M05 model. It is also worth nothing that the peak of the SFR distribution within the clump occurs at a higher SFR than in the spiral arm. The sSFR distributions in the clump are far more consistent among all the models, again showing a bimodal star formation in the clump, with one population peaking at $10^{-9.8}yr^{-1}$ and the other at $10^{-8.3}yr^{-1}$ as in the case of the spiral arm. The SFR and sSFR distributions imply that the star formation process in the spiral arm might be driven by the star formation in the clump itself.

Finally, in Figure 19, we examine clump B on the left side of the galaxy. Again, model differences affect primarily the SFR, with M05 predicting the SFR distribution to peak at $\sim 0.001 M_\odot \, yr^{-1}$ while BC03/CB07 predict that it peaks around 0.03 $M_\odot \, yr^{-1}$. Irrespective of the model, however, it is evident that the mean SFR of clump B is significantly lower than clump A, indicating that clump A is the primary driver of star formation in the outskirts of the galaxy. Despite some differences between M05 and the other models, therefore, pixel-z can be used to effectively and accurately probe mean properties of stellar popula-

tions within components of galaxies such as spiral arms and clumps. As discussed in section 1.1, this can be used to probe substructure in $z \sim 2$ galaxies in order to determine if these objects are largely driven by mergers or are disks formed in-situ.

3.6. *Incorporating WFC3 to Probe Substructure: Expectations from the CANDELS Survey*

Figure 20 shows the results of adding the NIR WFC3 imaging in the $F125W$ and $F160W$ passbands from the CANDELS survey to the existing $bviz$ bands for an example disk galaxy at $z = 0.6$, with the M05 models. The most notable difference between using the optical-only passbands and the combined optical and WFC3/NIR passbands is in the spatial distribution of the oldest ($t > 4$ Gyr) stellar populations in the galaxy. In the ACS-only case, the oldest stellar populations in the galaxy are confined in highly localized regions in the galaxy, with a concentration in the center and and in pockets in the southwest and sout-east of the image. The addition of the WFC3/NIR data, however, suggests that the oldest (and thus redder) populations are not simply confined in these pockets but are present more extensively in the disk itself. In the map of the specific star formation rate in the galaxy, both the optical-only and the combined optical and NIR cases suggest a qualitatively similar trend in the spatial distribution of the sSFR i.e., the sSFR is lowest in the center of the galaxy ($\sim 10^{-11} \, yr^{-1}$) and increases towards the outskirts. Away from the center, however, the addition of the WFC3/NIR passbands, suggests that the disk contains a higher proportion of stellar populations with a sSFR ($\sim 10^{-10} \, yr^{-1}$) that is lower than what is predicted by the optical-only colors. The differences observed in the maps of the stellar population age and sSFR are confirmed by the radial variation of these quantities, shown in Figure 21. The WFC3/NIR colors reveal an older population throughout the disk of the galaxy relative to the optical-only colors, with more than a 5σ difference in the luminosity-weighted mean age between the $bviz$ and $bvizJH$ colors and up to a radius of 6 kpc from the galaxy center, . The radial variation of the sSFR also reflects the fact that the WFC3/NIR colors are more sensitive to the older stellar population in the disk, which were otherwise not revealed by the ACS-only passbands. The WFC3/NIR colors reveal a lower sSFR at all radii compared to the ACS-only colors, although the difference is most significant between 3 and 5 kpc from the galaxy center.

4. SUMMARY

The pixel-z method performs SED-fitting to individual pixels in multicolor images of galaxies and obtains the values of stellar population properties, such as age, SFR, obscuration and metallicity, in the pixels. We use it to make detailed measurements of the properties of components in galaxies such as spiral arms and clumps as well as to measure the radial variation of star formation and other properties across galaxies. In this work, we present the application of the pixel-z technique to a sample of 467 resolved galaxies at $z \sim 1 - 3$ in the GOODS-South field in order to extract spatially resolved properties of these objects from their pixel colors. We have focused on the impact of systematic biases on how accurately this tech-

nique can probe substructure and stellar populations in these high redshift objects. We investigate various biases that affect the determination of stellar population properties within pixels. For each potential source of systematic error, we examine the distribution of the systematic error across all pixels in the galaxy sample. We also study the effect on the derived properties of components of galaxies. We summarize our findings below.

- Using optical-only passbands, we find that differences between population synthesis models can bias the derived stellar population properties, although the impact is minimal for the majority of pixels. The impact of differences between the BC03 and CB07 models are small, with over 94 percent of pixels in the galaxies having resulting systematic errors in their age, dust and τ properties that are below the statistical errors. However, a larger systematic uncertainty arises from differences between the M05 models and BC03/CB07 ones. This is likely related not to the differing prescriptions for TP-AGB stars but to other fundamental differences between the M05 models and the BC03/CB07 models. This causes systematic uncertainties in the pixel properties that impact a higher proportion of the pixels, resulting in an outlier fraction of pixels (with more than twice the statistical error) of approximately 0.15, 0.11 and 0.03 for the τ, stellar population age and color excess (dust obscuration) respectively.

- We explore systematic uncertainties in the stellar population properties within pixels resulting from a changing parameter space used by pixel-z. Increasing the range of parameter values that pixel-z searches is expected to exacerbate SED degeneracies. We find that when using the 4 optical bands, this systematic can be well controlled. The fractions of pixels whose stellar population parameters are affected in this manner are only 0.03, 0.06 and 0.01 for the τ, stellar population age and color excess respectively.

- We explore the effect of limiting the number of passbands available for the pixel-z analysis. We find that this results in the largest systematic errors in deriving stellar population properties in the pixels. Using 2 passbands alone results in large ($> 4\sigma$) systematic uncertainties in the parameters in the majority of the pixels. As expected, the more passbands that are available to sample the spectral range of the pixels, the more accurately stellar population parameters can be constrained. We find, however, that moderately robust results can be obtained with just three of the optical filters within the set of $bviz$, provided they are selected to span the 4000 Å break. We find that omitting one of the 4 optical passbands can bias (by more than twice the statistical error) the estimates in the stellar population age and τ in more than 20 percent of pixels in the sample. The SFR and the stellar population age are most impacted of all the stellar population properties by such limitations. Passband limitations are thus the largest source of systematic error in the pixel-z method.

- Using a subsample of 46 galaxies with near-infrared data from NICMOS/NIC3 camera, we study how systematic biases in the pixel-z parameters due to differences among stellar population synthesis models, are affected by the addition of the NIR passbands relative to the optical-only colors. The most important factor here is that the different models predict generally similar rest-frame UV colors but show significant differences in their predicted rest-frame NIR or optical (red) colors. Thus the impact of adding the NICMOS data has a redshift dependence. For the low redshift ($z < 1$) sample, the addition of the NIR passbands exposes differences in the rest-frame NIR colors among the three models being compared, and this impacts the stellar population age most strongly. For example, for BC03 and CB07, the fraction of pixels showing $< 1\sigma$ differences in age decreases from 0.89 with optical-only colors to 0.81 with NIR colors. However, for $z > 1$, the bias in the pixel-z parameters due to these model differences that arise from using NIR colors is not significantly different to those arising from using optical-only colors.

- We investigate any systematic difference between summing the SED fits to individual pixels in a galaxy (as done by pixel-z) and the global SED fit to the total flux in the same pixels within a fixed aperture. We find in general a good agreement between the SFR estimated by pixel-z and the one inferred from SED-fitting to the global photometry in the galaxy. While the majority of galaxies show differences in the SFR determined by the two methods which are smaller than the statistical uncertainties of the SFR measurements, we detect two small populations of galaxies with significant offsets. The first is in galaxies which show low SFR ($< 1M_\odot\, yr^{-1}$), where pixel-z estimates a higher SFR (by more than 2σ) than that determined by the global SED fit. A second small outlier population is found for galaxies showing SFR$\sim 10M_\odot\, yr^{-1}$, where the global SED fit to the total flux produces a higher SFR than that estimated by the sum of the individual SED fits.

- We show in some individual examples, that pixel-z can be robustly applied to substructure and stellar populations within components in galaxies at $z \sim 1 - 3$. We illustrate this with measurements of the radial variations of the age, obscuration, SFR and sSFR in these objects. We show that systematic uncertainties in these measurements that result from using different stellar population synthe-

sis models can generally be well constrained. In these examples, we find that the largest systematic differences arise between the M05 and BC03/CB07 models, when using optical-only passbands, as suggested by our statistical study on the full pixel and galaxy sample.

- We also show how pixel-z can be used to measure robustly the mean properties of components within disk galaxies such as spiral arms and clumps. Our results for individual galaxies suggests that pixel-z is generally robust to systematic errors from stellar population synthesis model differences in determining the distribution of age, dust obscuration and sSFR within these clumpy structures in high redshift disk galaxies.

It is important to note that, despite testing the above systematics, there are still several underlying implicit assumptions within pixel-z which may contribute systematic effects to inferred results on the stellar population parameters. These assumptions include independent pixels, independent stellar populations in each pixel and star formation histories that are described by a single burst and exponential decline. These are likely to have less impact when the statistical properties of large populations of galaxies (and pixels) are investigated. In order to address the impact of these assumptions rigorously, a detailed comparison of this technique against spatially resolved spectroscopic observations for a large sample of galaxies (as proposed by Croom et al. 2011) will be required. Comparison with such IFU observations for a large sample of galaxies will enable a calibration of the pixel-z method and an eventual refinement of these assumptions.

REFERENCES

Agertz, O., Teyssier, R., & Moore, B. 2009, MNRAS, 397, L64
Alard, C. & Lupton, R.H., 1998, ApJ, 503, 325
Alard, C., 1999, arXiv:astro-ph/9903111
Bacon, R., et al., 2001, MNRAS, 326, 23
Balestra, I., et al., 2010, A&A, 512, 12
Blanton, M. R., et al., 2005, ApJ, 631, 208
Bournaud, F., Elmegreen, B.G., Elmegreen, D.M., et al., 2007, ApJ, 670, 237
Bournaud, F., et al., 2008, å, 486, 741
Bouwens, R.J., et al., 2010, ApJ, 725, 1587
Bruzual, G., & Charlot, S., 2003, MNRAS, 344, 1000

Cameron, E., et al., 2010, arXiv:astro-ph/1007.2442
Cardamone, C.N., 2010, ApJS, 189, 270
Casertano, S., et al., 2000, AJ, 120, 2747
Ceverino, D., Dekel, A., & Bournaud, F. 2010, MNRAS, 404, 2151
Conselice, C.J., et al., 2011, MNRAS, 413, 80
Conti, A., et al., 2003, AJ, 126, 2330
Contini et al., 2011, submitted
Cooper at al., 2007, MNRAS, 376, 1445
Croom. S. M., et al., 2011, in preparation
Cucciati, O., et al., 2006, A&A458, 39
Daddi, E., et al., 2010, ApJ, 713, 686

Dekel, A., Sari, R., & Ceverino, D. 2009, ApJ, 703, 785
Driver, S.P., et al., 2011, MNRAS, 413, 971
Elbaz, D., et al., A&A, 468, 33
Elmegreen, D. M., et al., 2007, ApJ, 658, 763
Elmegreen, D. M., et al., 2008, ApJ, 688, 67
Elmegreen, D. M., et al., 2009, ApJ, 692, 12
Epinat et al., 2011, submitted
Förster Schreiber, N. M., et al. 2006, ApJ, 645, 1062
Förster Schreiber, N. M., et al. 2011a, ApJ, 731, 65
Förster-Schreiber, N. M., et al. 2011b, ApJ, 739, 45
Genzel, R., et al. 2006, Nature, 442, 786
Genzel, R., et al., 2008, ApJ, 687, 59
Genzel, R., et al., 2011, ApJ, 733, 101
Giavalisco, M., et al., 2004, ApJ, 600, 103
Girardi, L., et al., 2000, A&AS, 141, 371
Gomez, P. L., et al., 2013, ApJ, 584, 210
Grogin, N. A., Kocevski, D. D., Faber, S. M., et al., 2011, ApJS, 197,
    35
Grützbauch, R., et al., 2011, MNRAS, 411, 929
Hogg, D. W., et al., 2004, ApJ, 601, 29
Ideue, Y., et al., 2009, ApJ, 700, 971
Ilbert, O., et al., 2006, arXiv:astro-ph/0602329
Immeli, A., et al., 2004a, A&A, 413, 547
Immeli, A., et al., 2004b, ApJ, 611, 20
Johnston, H. M., et al., 2005, MNRAS, 356, 515
Kassin, S. A., et al., 2003, AJ, 126, 1276
Koekemoer, A. M., Faber, S. M., Ferguson, H., et al., 2011, ApJS,
    197, 36
Lanyon-Foster, M. M., et al., 2007, MNRAS, 380, 571
Law, D. R., et al., 2007, ApJ, 656, 1
Lotz, J. M., et al., 2004, AJ, 128, 163
Lotz, J. M., et al., 2006, ApJ, 636, 592

Magee, D.K., Bowens, R.J., & Illingworth, G.D., 2007, in ASP Conf.
    Ser. 376, Astronomical Data Analysis Software and Systems XVI,
    ed. R. A. Shaw, F. Hill, & D. J. Bell (San Francisco: ASP), 261i
Maraston, C., 2005, MNRAS, 362, 799
Maraston, C., 2006, ApJ, 652, 85
Noguchi, M., et al., 1999, ApJ, 514, 77
Overzier, R.A., et al., 2010, ApJ, 710, 979
Pannella, M., et al., 2009, ApJ, 701, 787
Park, C., et al., 2007, ApJ, 658, 898
Patel, S., et al., 2011, ApJ, 735, 53
Peng, C.Y., et al., 2002, AJ, 124, 266
Peng, C.Y., et al., 2010, AJ, 139, 2097
Peng, Y., et al., 2010, ApJ, 721, 193
Poggianti, B.M., et al., 2006, ApJ, 642, 188
Popesso, P., et al., 2009, A&A, 494, 443
Quadri, R.F., 2011, arXiv:astro-ph/1104.1426
Queyrel et al., 2011, submitted
Robertson, B. E., & Bullock, J. S. 2008, ApJ, 685, L27
Salimbeni, S., et al., 2009, A&A, 501, 865
Sanchez, S. F., et al., 2011, arXiv:astro-ph:1111.0962
Scarlata, C., et al., 2007, ApJS, 172, 406
Scodeggio, M., et al., 2009, A&A, 501, 21
Tacconi, L. J., et al., 2010, Nature, 463, 781
Toft, S., et al., 2007, ApJ, 671, 285
Tran, K.H., et al., 2010, ApJ, 719, 126
Welikala, N., et al., 2008, ApJ, 677, 970
Welikala, N., et al., 2009, ApJ, 701, 994
Welikala, N., et al., 2011, in preparation
Wijeshinghe, D., 2011, in preparation
Worthey, G., et al., 1994, ApJS, 94, 687
Zibetti, S., & Groves, B., 2011, MNRAS, 417, 812

	[BC03,CB07]		[BC03,M05]		[CB07,M05]	
	$< 1\sigma$	$> 2\sigma$	$< 1\sigma$	$> 2\sigma$	$< 1\sigma$	$> 2\sigma$
τ	0.94	0.03	0.71	0.15	0.80	0.17
age	0.94	0.04	0.86	0.11	0.87	0.11
$E(B-V)$	0.99	0.01	0.95	0.03	0.94	0.03

TABLE 1

EFFECT OF STELLAR POPULATION SYNTHESIS MODELS. SHOWN FOR EACH PIXEL-z INFERRED PARAMETER (ROW) IS THE FRACTION OF PIXELS WITH SYSTEMATIC DIFFERENCES OF (A) $< 1\sigma$ AND (B) $> 2\sigma$ FOR EACH OF THE PAIRS OF MODELS THAT WERE COMPARED.

	$< 1\sigma$	$> 2\sigma$
τ	0.94	0.03
age	0.92	0.06
E(B-V)	0.99	0.01

TABLE 2

EFFECT OF INCREASING THE METALLICITY RANGE, AND CONSEQUENTLY THE NUMBER OF SEDS FROM 2178 TO 4356, IN THE PIXEL-z GRID. SHOWN FOR EACH INFERRED PIXEL-z PARAMETER IS THE FRACTION OF PIXELS WITH SYSTEMATIC DIFFERENCES OF $< 1\sigma$ AND $> 2\sigma$.

	$[b+i+z]$		$[b+v+i]$		$[v+i+z]$	
	$< 1\sigma$	$> 2\sigma$	$< 1\sigma$	$> 2\sigma$	$< 1\sigma$	$> 2\sigma$
τ	0.72	0.20	0.65	0.26	0.73	0.20
age	0.70	0.28	0.71	0.26	0.76	0.22
$E(B-V)$	0.82	0.11	0.78	0.13	0.78	0.14

TABLE 3

EFFECT OF PASBAND LIMITATIONS. SHOWN FOR EACH PIXEL-z INFERRED PARAMETER IS THE FRACTION OF PIXELS IN THE FULL SAMPLE OF 467 GALAXIES WHICH HAVE SYSTEMATIC DIFFERENCES OF $< 1\sigma$ AND $> 2\sigma$ AS A RESULT OF DIFFERENT PERMUTATIONS OF AVAILABLE BROADBAND FILTERS.

	[BC03,CB07]		[BC03,M05]		[CB07,M05]	
	$bviz$	$bvizJH$	$bviz$	$bvizJH$	$bviz$	$bvizJH$
τ	0.98	0.88	0.84	0.81	0.83	0.81
age	0.98	0.78	0.89	0.80	0.89	0.80
$E(B-V)$	0.99	0.91	0.96	0.94	0.97	0.92

TABLE 4

COMPARING THE LEVEL OF AGREEMENT BETWEEN PAIRS OF STELLAR POPULATION SYNTHESIS MODELS WHEN USING OPTICAL COLORS ONLY WITH THOSE ARISING FROM USING OPTICAL AND NIR COLORS, FOR A SAMPLE OF GALAXIES AT $z \leq 1$ WITH $bviz$ AND JH IMAGING. LISTED ARE THE FRACTION OF ALL PIXELS IN THIS LOW REDSHIFT GALAXY SAMPLE WHICH SHOW SYSTEMATIC DIFFERENCES SMALLER THAN 1σ IN THEIR PIXEL-z PARAMETERS.

	[BC03,CB07]		[BC03,M05]		[CB07,M05]	
	$bviz$	$bvizJH$	$bviz$	$bvizJH$	$bviz$	$bvizJH$
τ	0.95	0.96	0.78	0.80	0.80	0.82
age	0.99	0.97	0.95	0.93	0.96	0.92
$E(B-V)$	0.99	0.99	0.95	0.90	0.95	0.91

TABLE 5

COMPARING THE LEVEL OF AGREEMENT BETWEEN PAIRS OF STELLAR POPULATION SYNTHESIS MODELS WHEN USING OPTICAL COLORS ONLY WITH THOSE ARISING FROM USING OPTICAL AND NIR COLORS, FOR A SUBSAMPLE OF GALAXIES AT $z > 1$ WITH $bviz$ AND JH IMAGING. LISTED ARE THE FRACTION OF ALL PIXELS IN THE LOW REDSHIFT GALAXY SAMPLE WHICH SHOW SYSTEMATIC DIFFERENCES SMALLER THAN 1σ IN THEIR PIXEL-z PARAMETERS.
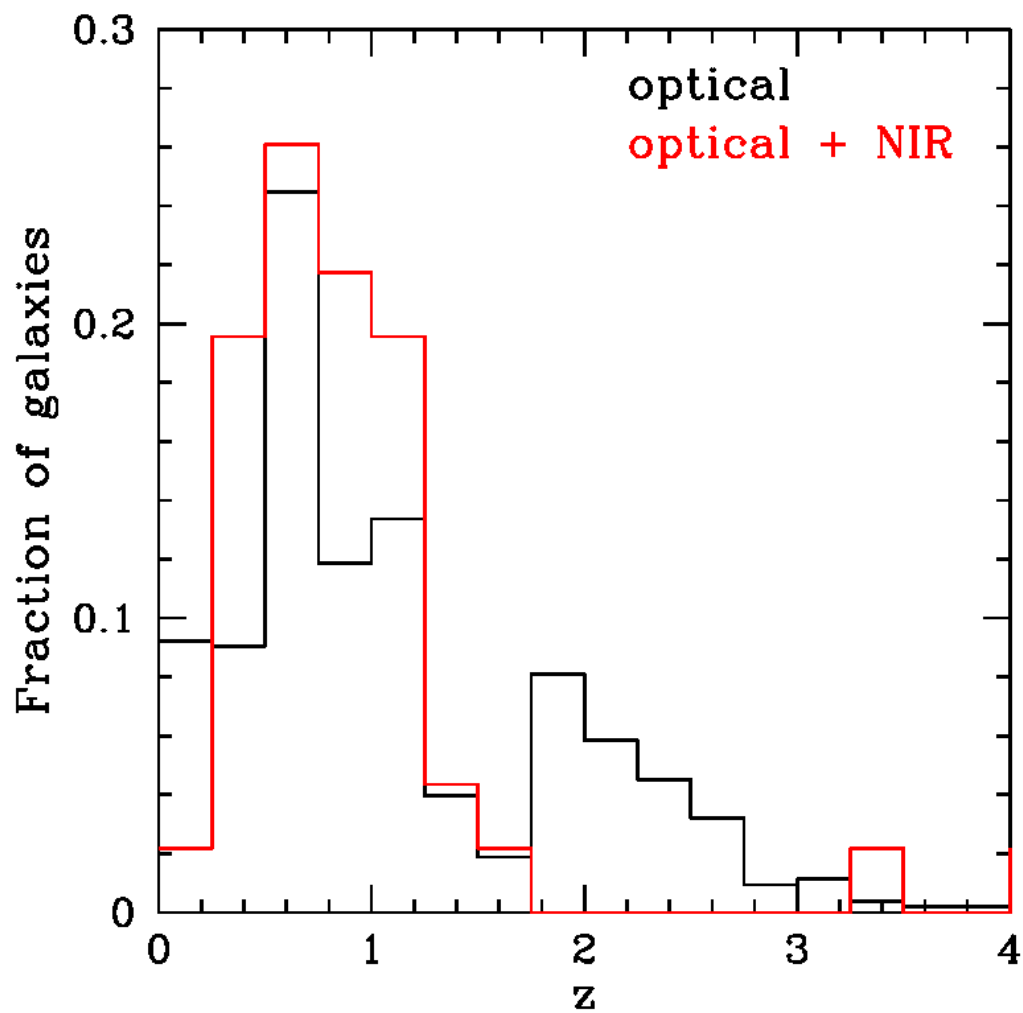
FIG. 1.— The redshift distribution of (a) the optical sample of 467 galaxies with *bviz* imaging (black) and (b) the subsample of 46 galaxies with near-infrared imaging from NIC3 (red).
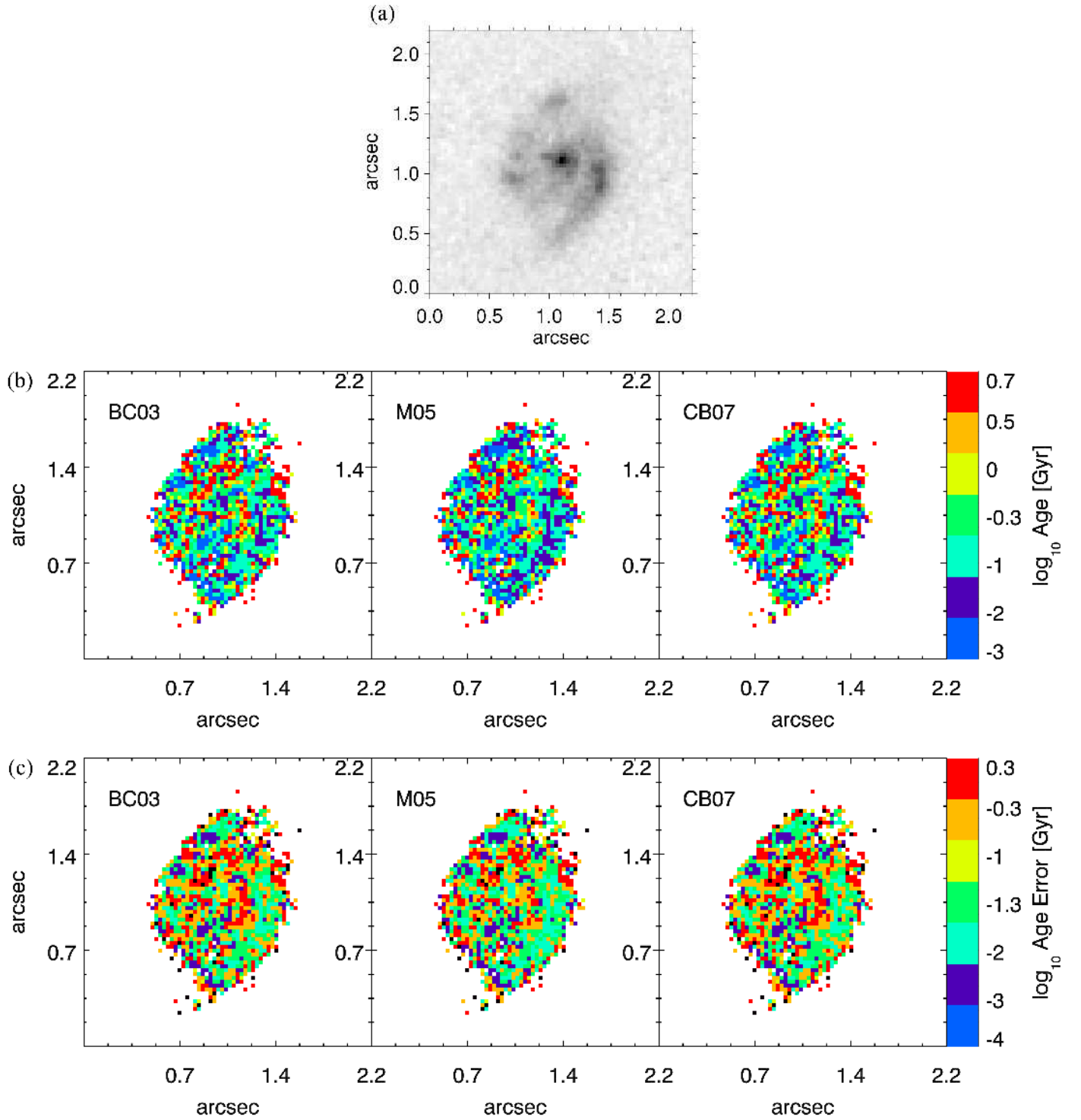
Fig. 2.— Illustration of the small effect of the chosen stellar population model in extracting stellar population properties from the pixel colors. Four optical bands ($bviz$) were used in this galaxy at $z = 1.05$. (a) i band image (b) stellar population age decomposition for BC03, CB07 and M05 population synthesis models (2178 spectra in each model) (c) Error in the stellar population age for the same models.
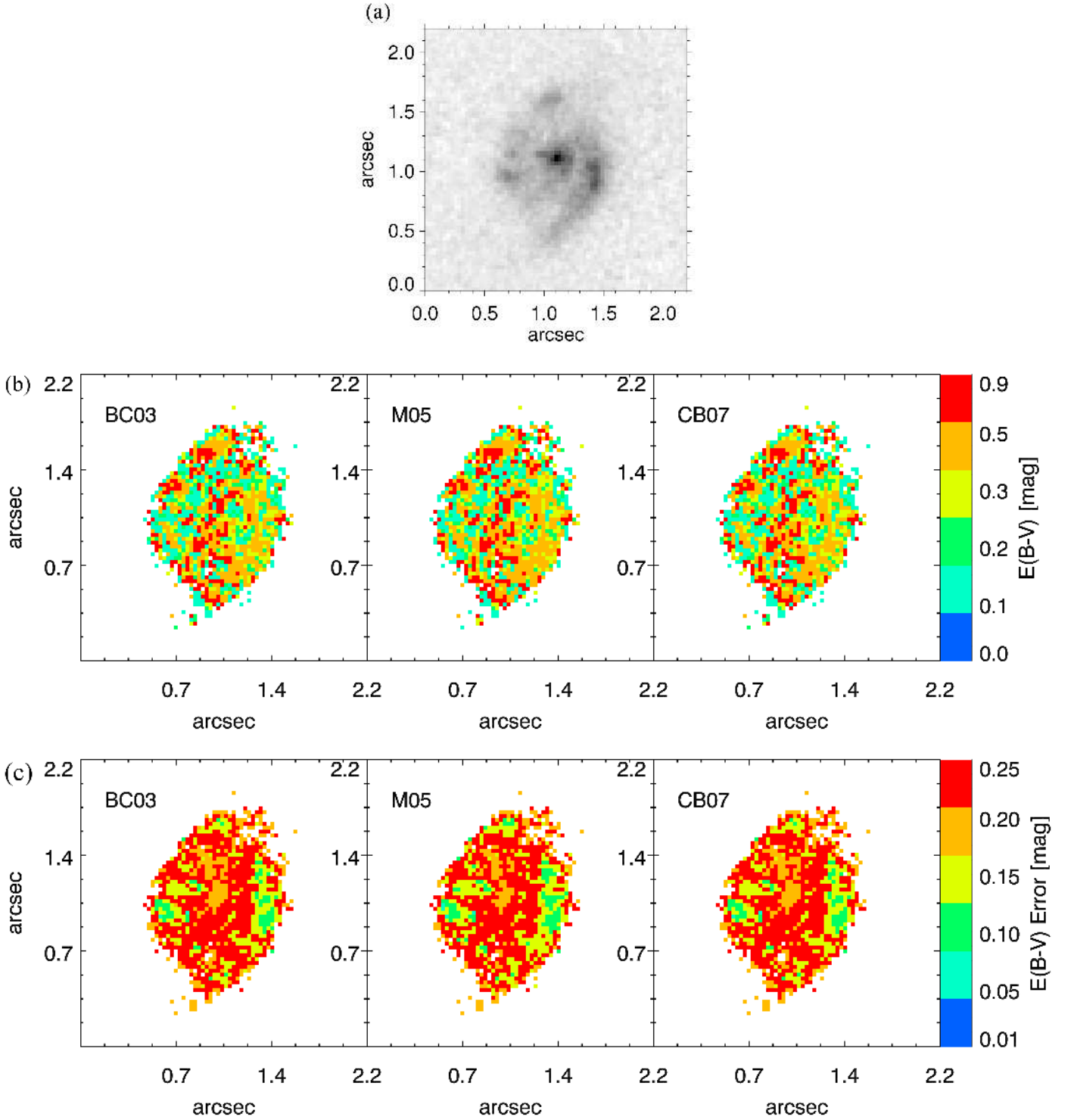
FIG. 3.— Illustration of the small effect of the chosen stellar population model in extracting stellar population properties from the pixel colors. Four optical bands ($bviz$) were used in this galaxy at $z = 1.05$. (a) i band image. (b) Dust obscuration decomposition (given in terms of $E(B-V)$) for BC03, CB07 and M05 population synthesis models (2178 spectra in each model) (c) Error in $E(B-V)$ for the same models.
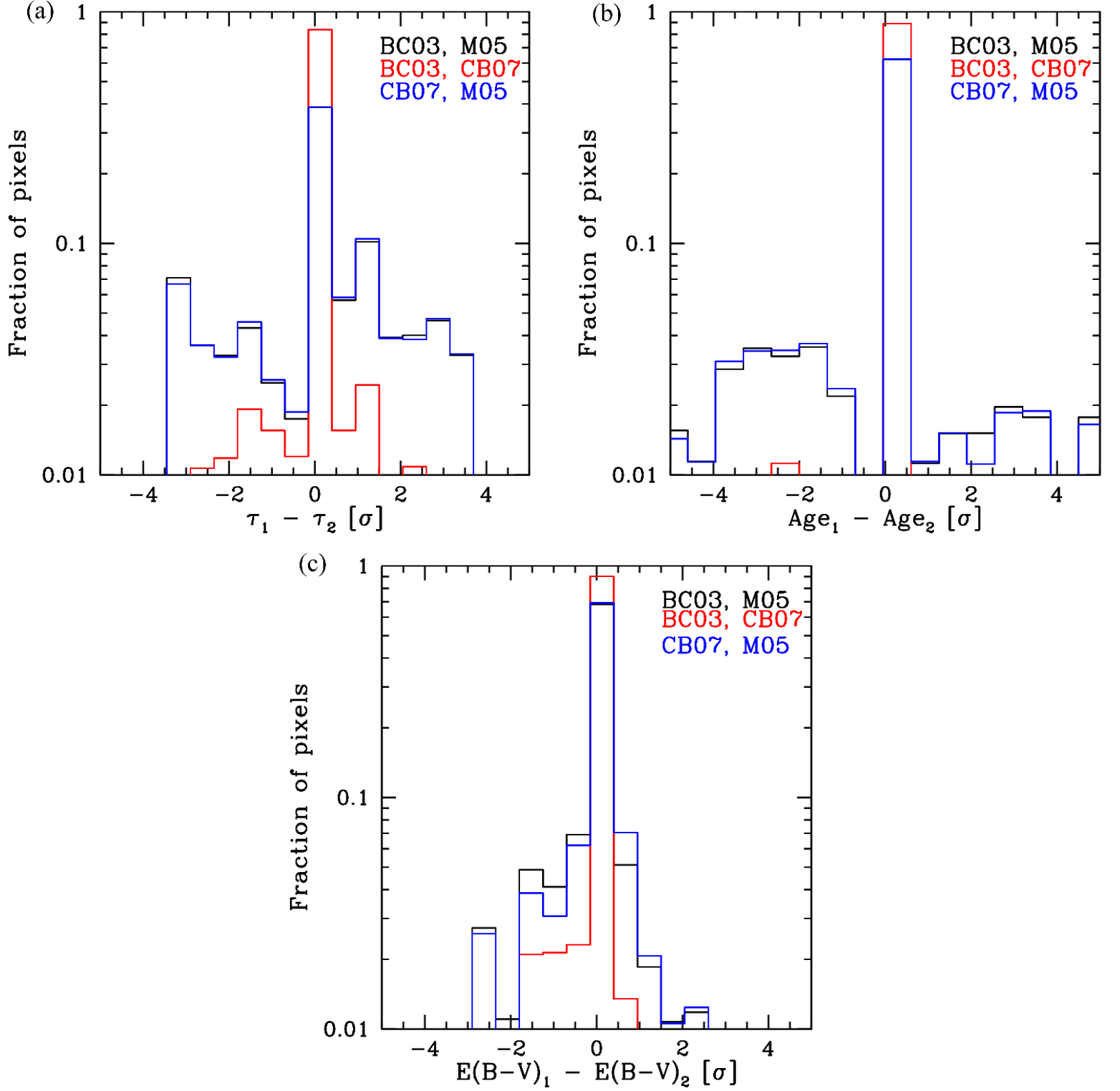
Fig. 4.— Quantifying the effect of stellar population synthesis models (in terms of the statistical error) for all the pixels in the 467 galaxies, selected to have half light radii $R_{50} > 0.5''$ and measured spectroscopic redshifts. We plot in each panel the distribution of the systematic error in the pixel-z parameter (due to model differences) in terms of the statistical error (σ) in that parameter, for all the pixels in the sample. (a) SFR e-folding time, (b) age of the stellar population and (c) dust obscuration shown in terms of $E(B-V)$. The pairs of models compared in each panel are: BC03 and M05 (black), BC03 and CB07 (red) and CB07 and M05 (blue). Only pixels within $2R_{50}$ are considered.
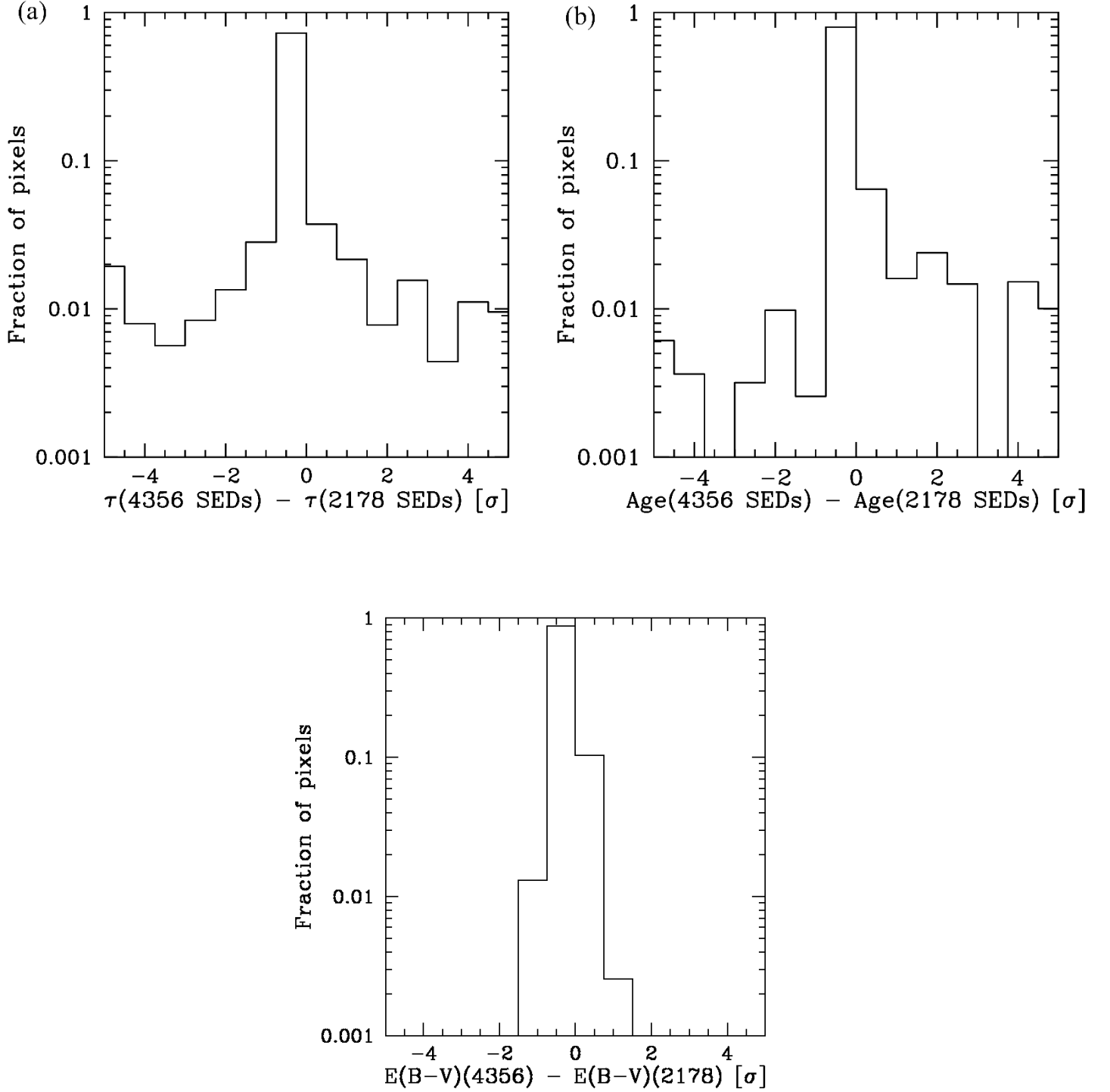
FIG. 5.— Effect of increasing the range of metallicity values (and hence the number of SEDs) allowed for the BC03 models for all pixels in the entire galaxy sample of 467 objects. Here we fix the model (BC03) and examine the effect of increasing the range of metallicity values from 3 allowed metallicities (resulting in a total of 2178 SEDs) to 6 allowed values (4356 SEDs). Shown in each panel is the distribution of the systematic error in the recovered pixel-z parameter in terms of the statistical error (σ) in the parameter, for all pixels in the sample: (a) SFR e-folding time (b) stellar population age and (c) dust obscuration given in terms of $E(B - V)$. Only pixels within $2R_{50}$ are considered.
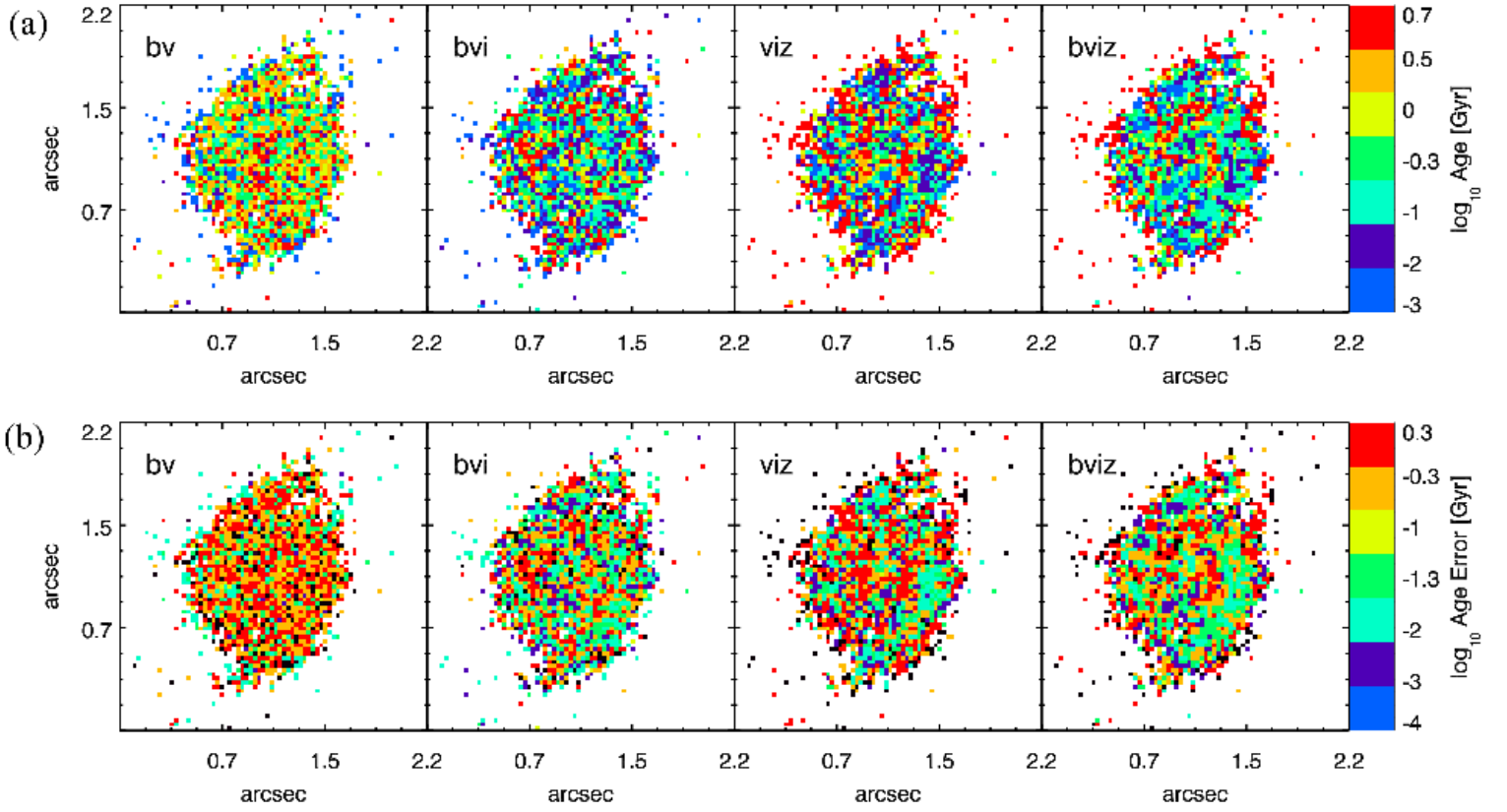
FIG. 6.— Systematic effect of passband changes on the stellar population age map for the galaxy shown in Figures 2 and 3. The stellar population synthesis model used here is BC03. (a) Map of the stellar population age for the galaxy for the following passband combinations: (b+v), (b+v+i), (v+i+z), (b+v+i+z). (b) Map of the error in the stellar population age for the same passband combinations.
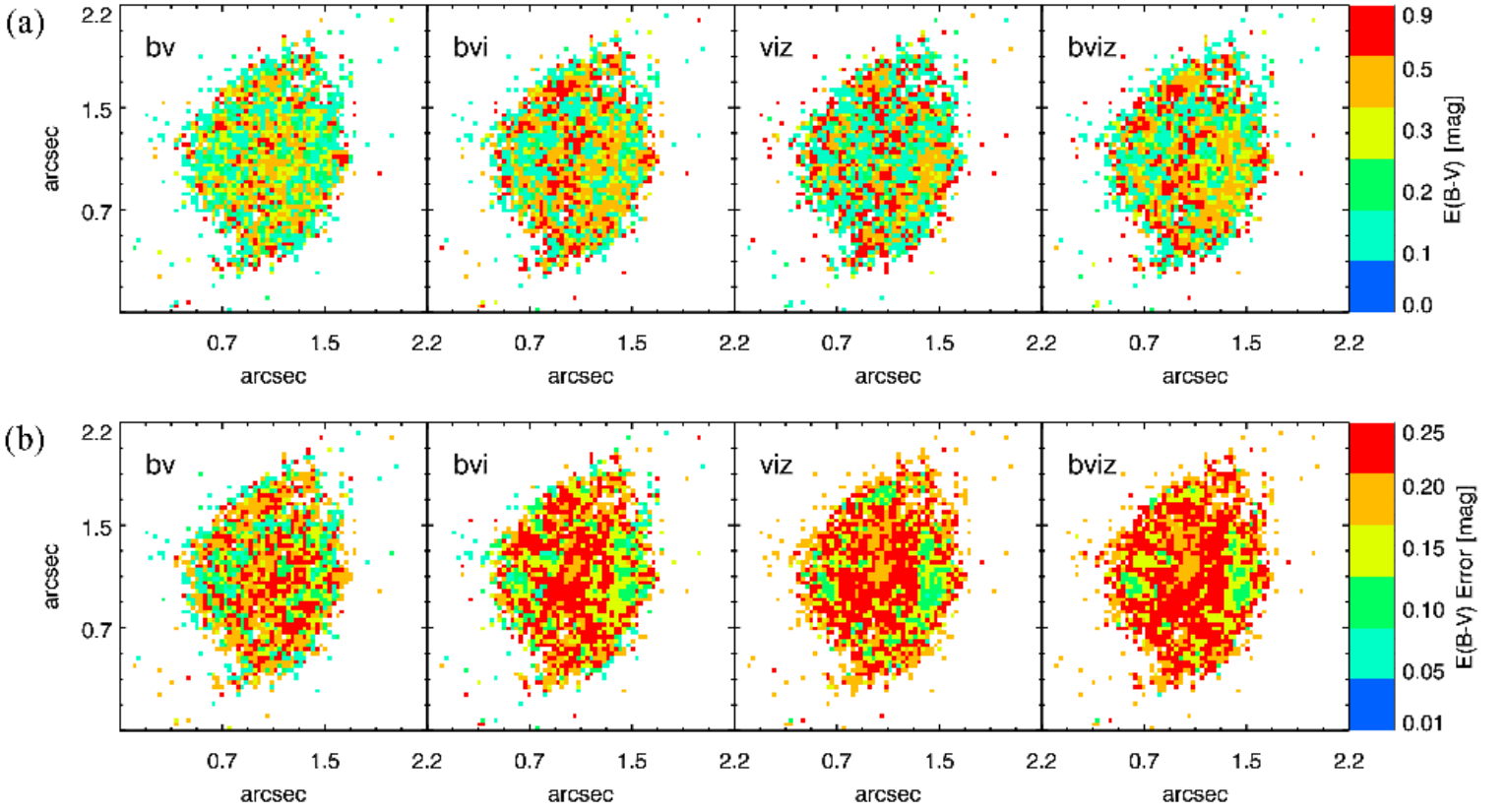
Fig. 7.— Systematic effect of passband changes on the dust obscuration map of the galaxy shown in Figures 2 and 3. The stellar population synthesis model used here is BC03. (a) Map of the $E(B-V)$ for the galaxy for the following passband combinations: (b+v), (b+v+i), (v+i+z), (b+v+i+z). (b) Map of the error in $E(B-V)$ for the same passband combinations.
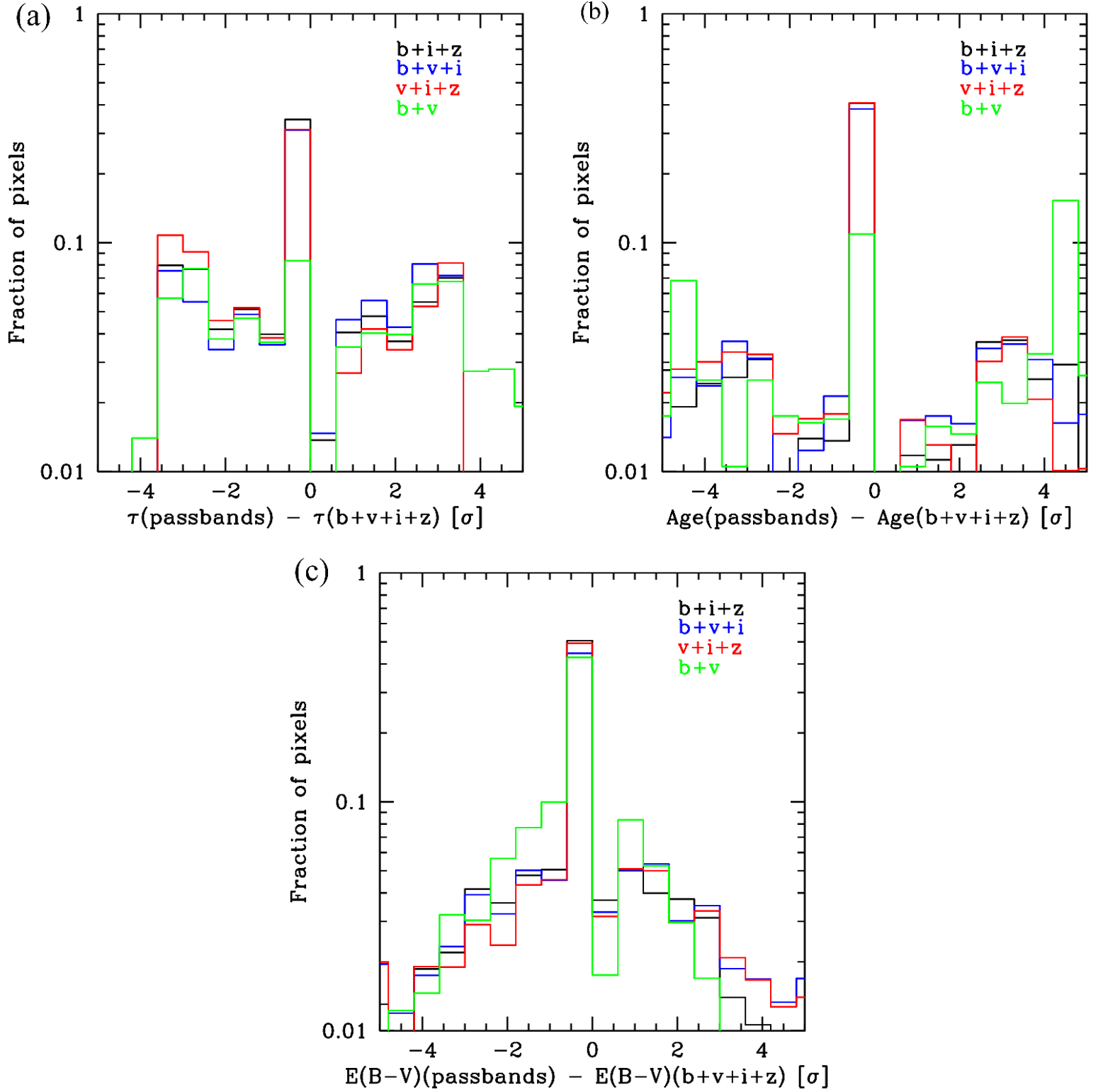
Fig. 8.— Systematic effect of passband changes for all the pixels in the entire galaxy sample, with a fixed stellar population synthesis model (BC03). Shown is the distribution of the systematic error in the parameters (given in terms of the statistical error σ) that arise from omitting passbands relative to the full complement of optical bands ($bviz$). The systematic error is measured for (a) the SFR e-folding time (b) stellar population age and (c) the dust obscuration given in terms of $E(B-V)$. For each parameter, the passbands considered are: biz (black), bvi (blue) and viz (red). For illustrative purposes, we also plot, for only the single galaxy shown in Figures 2 and 3, the distribution of the systematic error resulting from using only the 2 passbands bv (green).
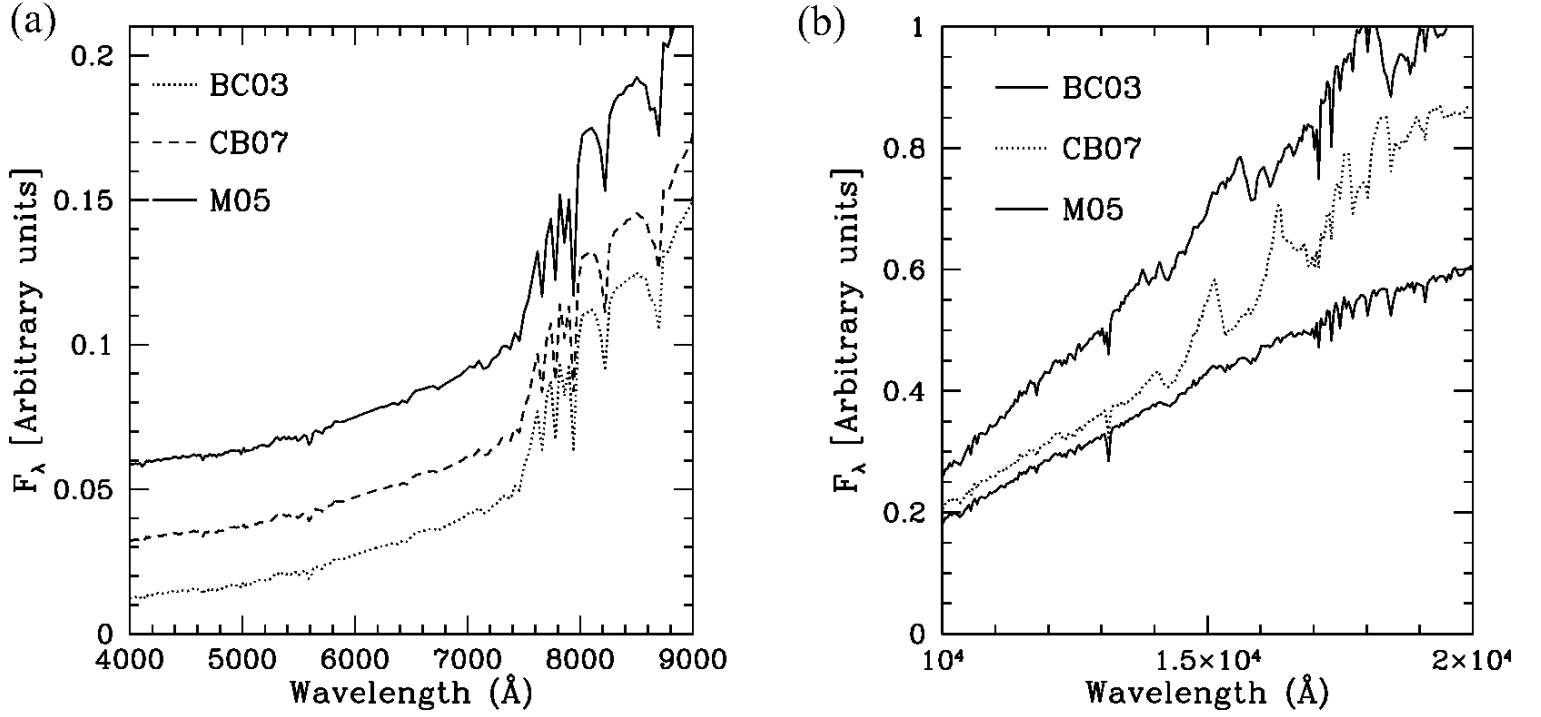
Fig. 9.— (a) Example SEDs in the optical spectral range of a galaxy at redshift=1.0, age = 3 Gyr, tau = 10 Gyr, E(B-V)=0.9 and Z = 0.008. There is very little difference in the shape of the continuum among the BC03, CB07 and M05 stellar population synthesis models in the optical. (b) The SEDs of the same galaxy in the NIR, where differences in the shape of the continuum emerge among the three models. These will give rise to different predicted NIR colors.
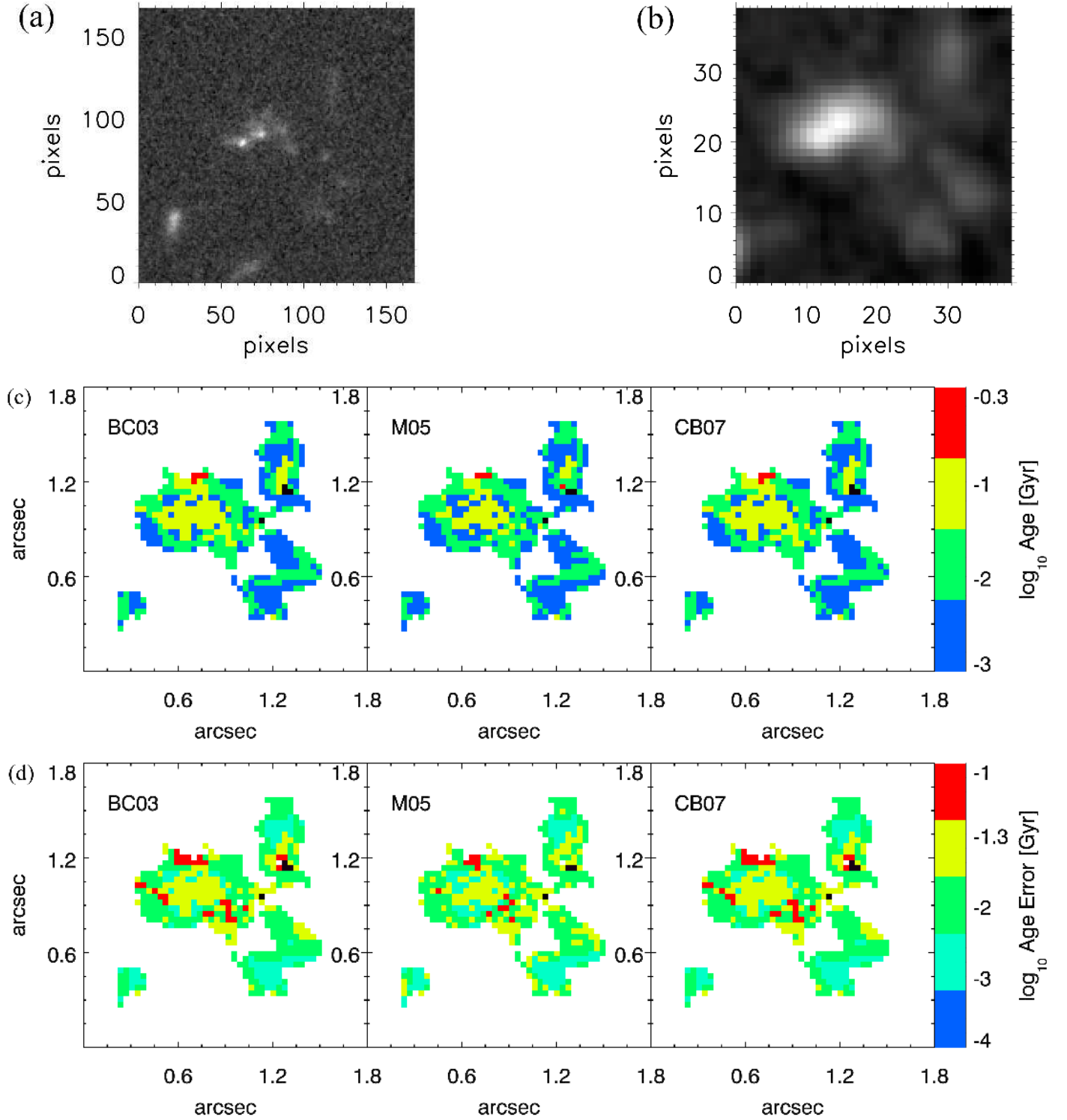
FIG. 10.— Spatial distribution of the stellar population age in a $z = 2.5$ galaxy after adding NIR colors to the pixel-z analysis. The galaxy was detected in both GOODS-South and the GOODS-NICMOS survey. It has an irregular morphology and has two associated companions on the right of the image. In total, 6 passbands ($bvizJH$) are used. (a) the original i band image of the galaxy (b) i band image of the galaxy after resampling and PSF-matching to the $F160W$ image of the galaxy (c) map showing the distribution of the stellar population age inferred from the BC03, M05 and CB07 stellar population synthesis models (d) map showing the the error in the age for the same models.
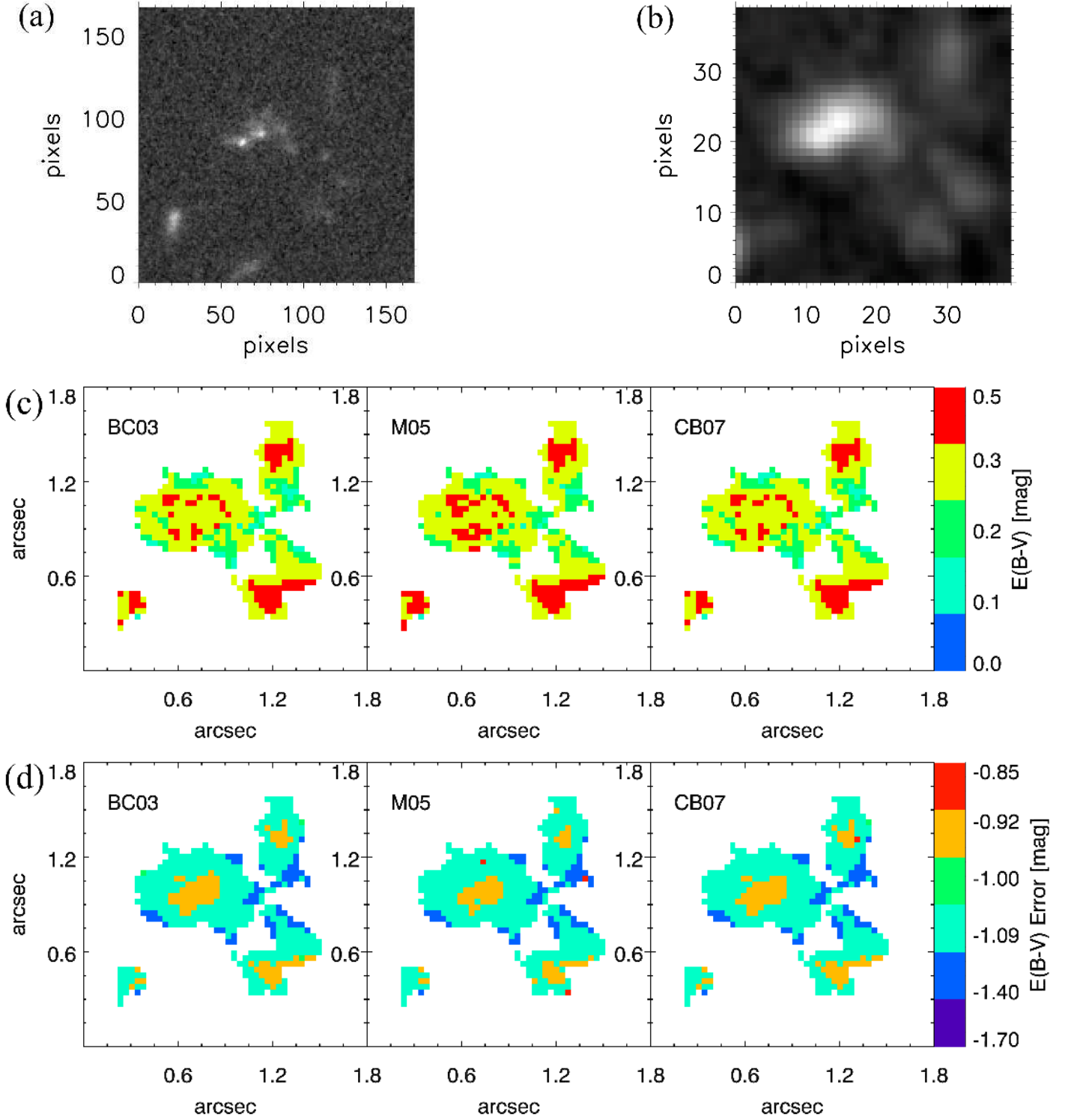
FIG. 11.— Spatial distribution of dust obscuration in a $z = 2.5$ galaxy and its companions after adding NIR colors to the pixel-z analysis. The galaxy was detected in both GOODS-South and the GOODS-NICMOS survey. It has an irregular morphology and has two associated companions on the right of the image. In total, 6 passbands ($bvizJH$) are used (a) the original i band image of the galaxy (b) i band image of the galaxy after resampling and PSF-matching to the $F160W$ image of the galaxy (c) map showing the distribution of the dust obscuration (in terms of $E(B - V)$) inferred from the BC03, M05 and CB07 stellar population synthesis models (d) map showing the the error in the $E(B - V)$ for the same models.
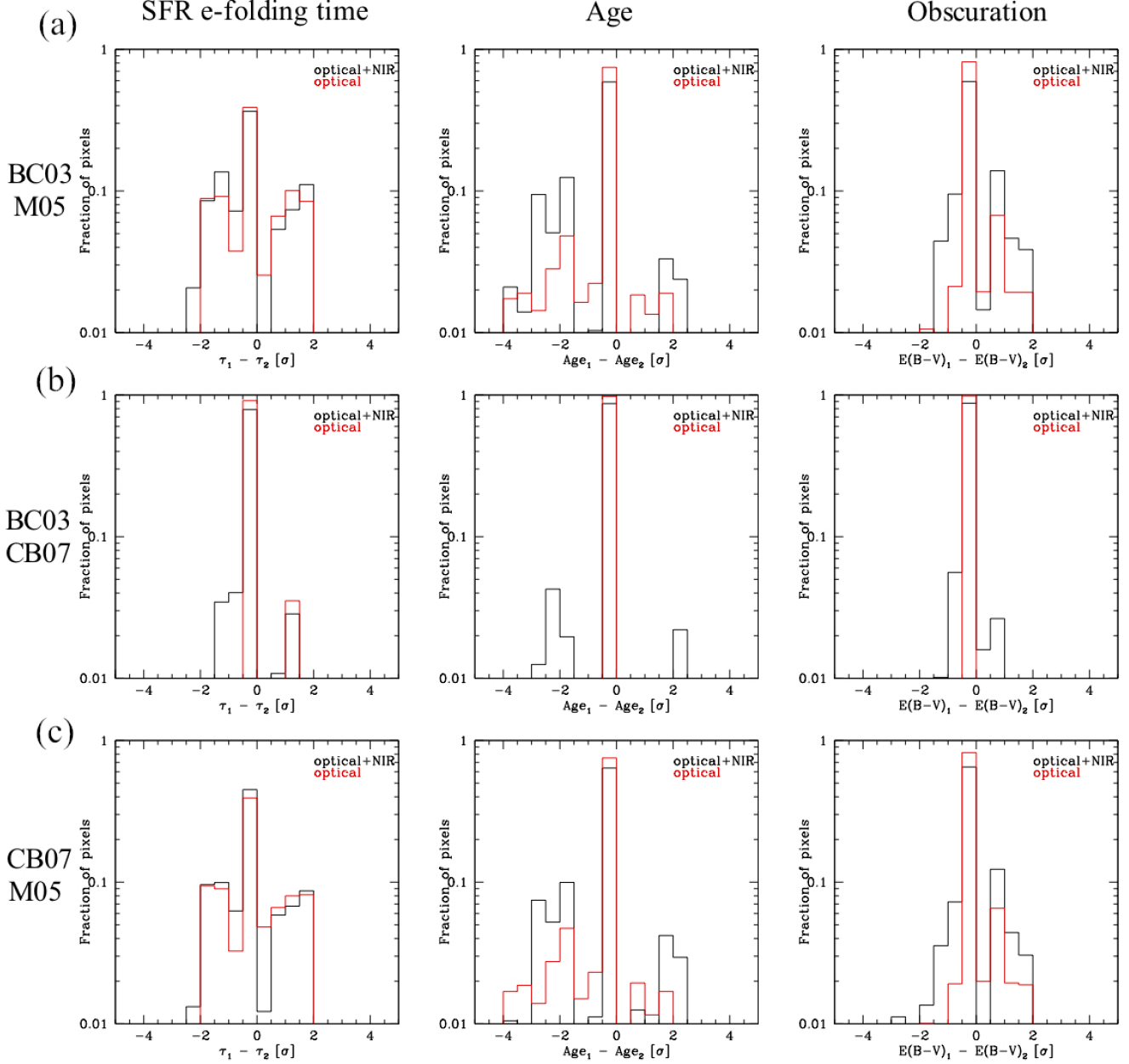
Welikala et al.
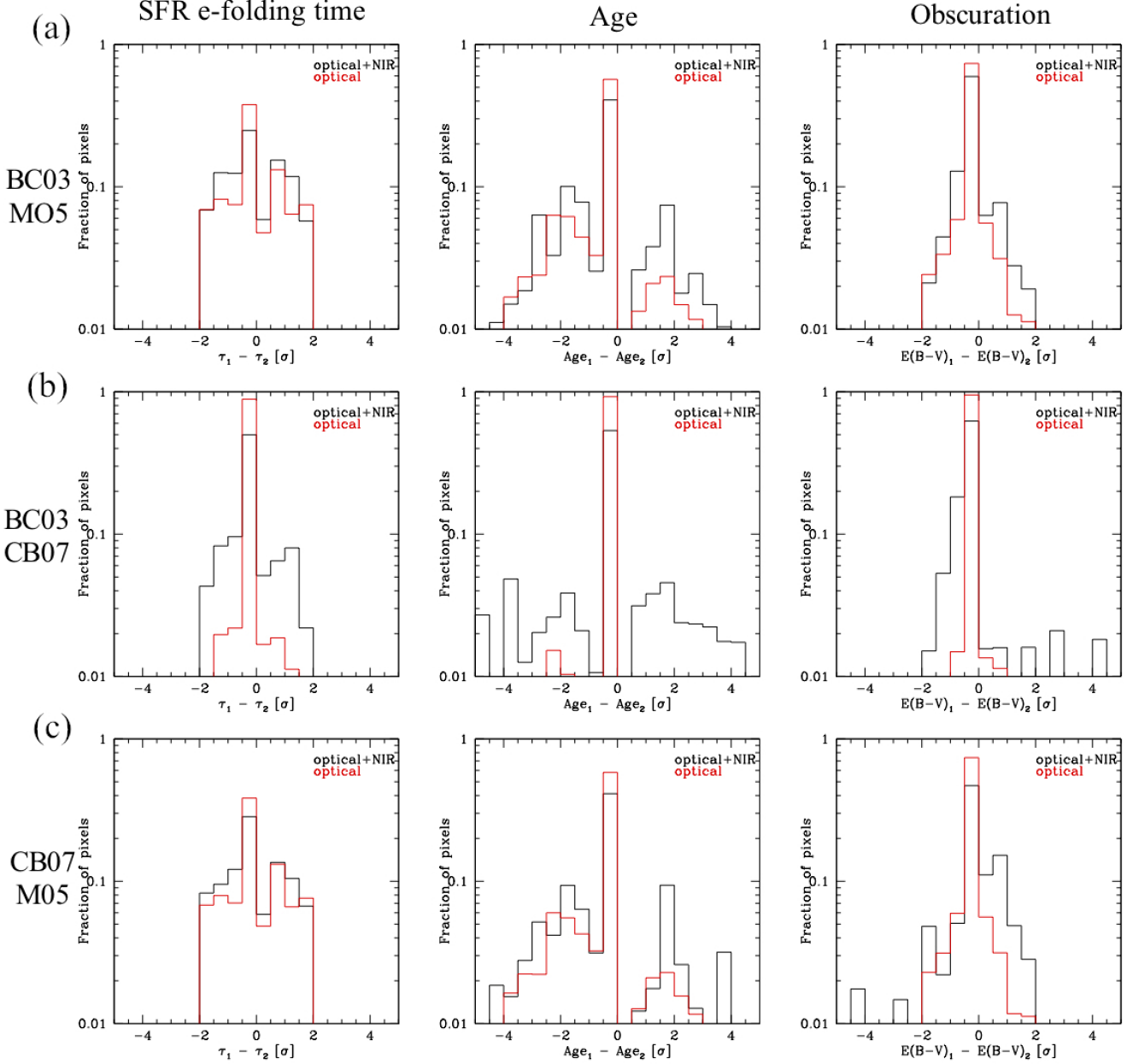
Fig. 12.— The effect of adding NIR passbands on the systematic differences between stellar population synthesis models, for pixels in a subsample of $z \leq 1$ galaxies. Shown are the distributions of systematic differences in the pixel-z parameters (given in terms of the statistical error σ) between pairs of population synthesis models when using optical-only colors (in red) and optical and NIR colors (in black). We consider all pixels in this subsample of $z \leq 1$ galaxies which have J and H as well as optical imaging. The distribution of these systematic differences between each pair of models is investigated for the SFR e-folding time, stellar population age and dust obscuration. The pairs of models being compared for each pixel-z parameter are: (a) BC03 and M05, (b) BC03 and CB07 and (c) CB07 and M05.

FIG. 13.— The effect of adding NIR passbands on the systematic differences between stellar population synthesis models, for pixels in a subsample of $z > 1$ galaxies. Shown are the distribution of systematic differences (given in terms of the statistical error σ) in the pixel-z parameters between pairs of population synthesis models when using optical-only colors (in red) and optical and NIR colors (in black). We consider all pixels in this subsample of $z > 1$ galaxies which have J and H as well as optical imaging. The distribution of these systematic differences between each pair of models is investigated for the SFR e-folding time, stellar population age and dust obscuration. The pairs of models being compared for each pixel-z parameter are: (a) BC03 and M05, (b) BC03 and CB07 and (c) CB07 and M05.
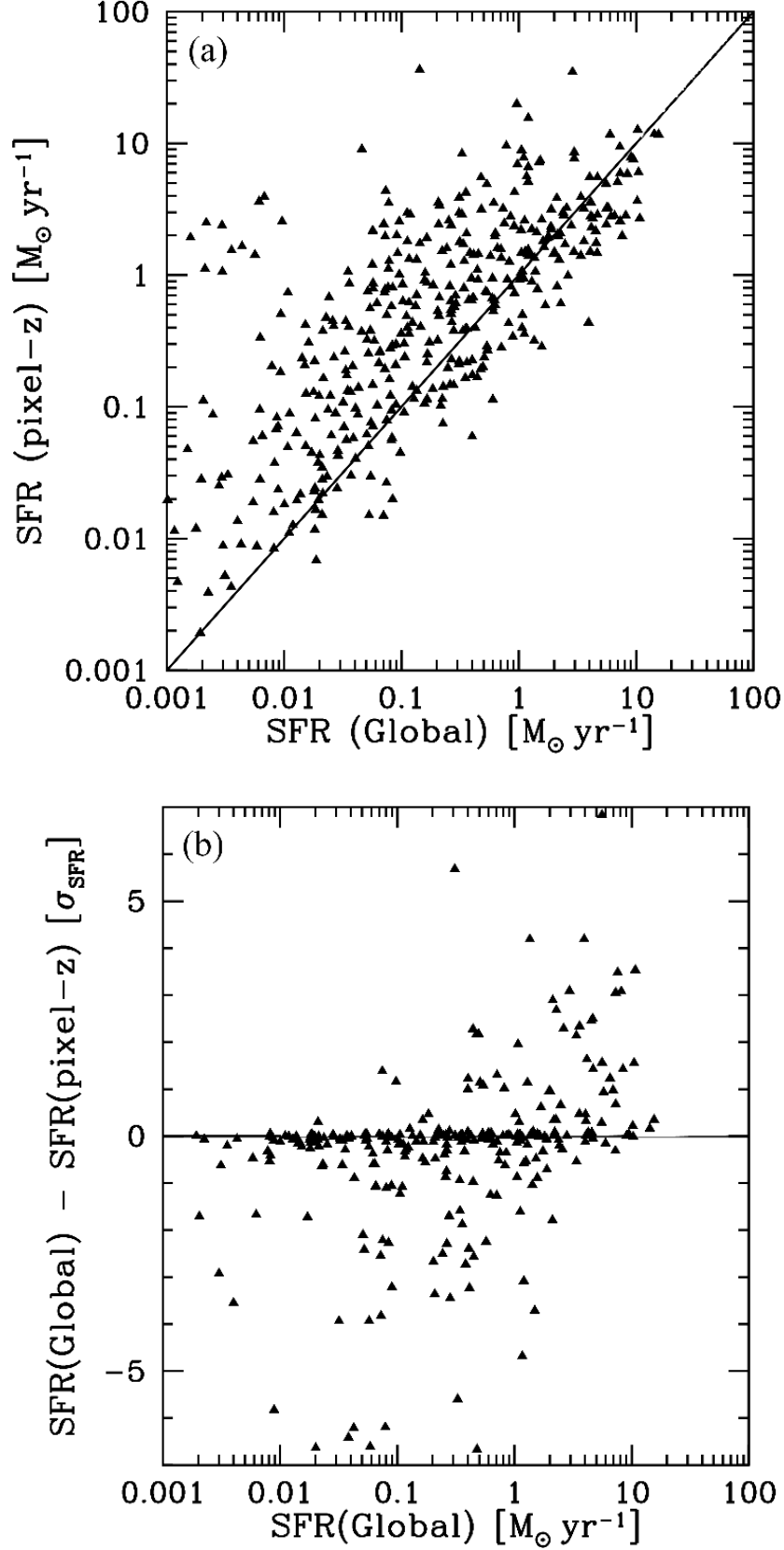
FIG. 14.— Comparison of the sum of SED fits to the individual colors in pixels in each galaxy (as found by pixel-z) with the SFR derived from global SED-fitting to the integrated colors of the galaxy. For each galaxy, the same pixels within a 0.5" aperture were used in both approaches. (a) The total SFR of galaxies derived from pixel-z as a function of the SFR derived from the global SED fit to the integrated colors in the galaxies. (b) The residual difference between the two approaches, given in terms of the statistical error in the SFR measurement of the galaxy, as a function of the SFR derived from the global SED fit.
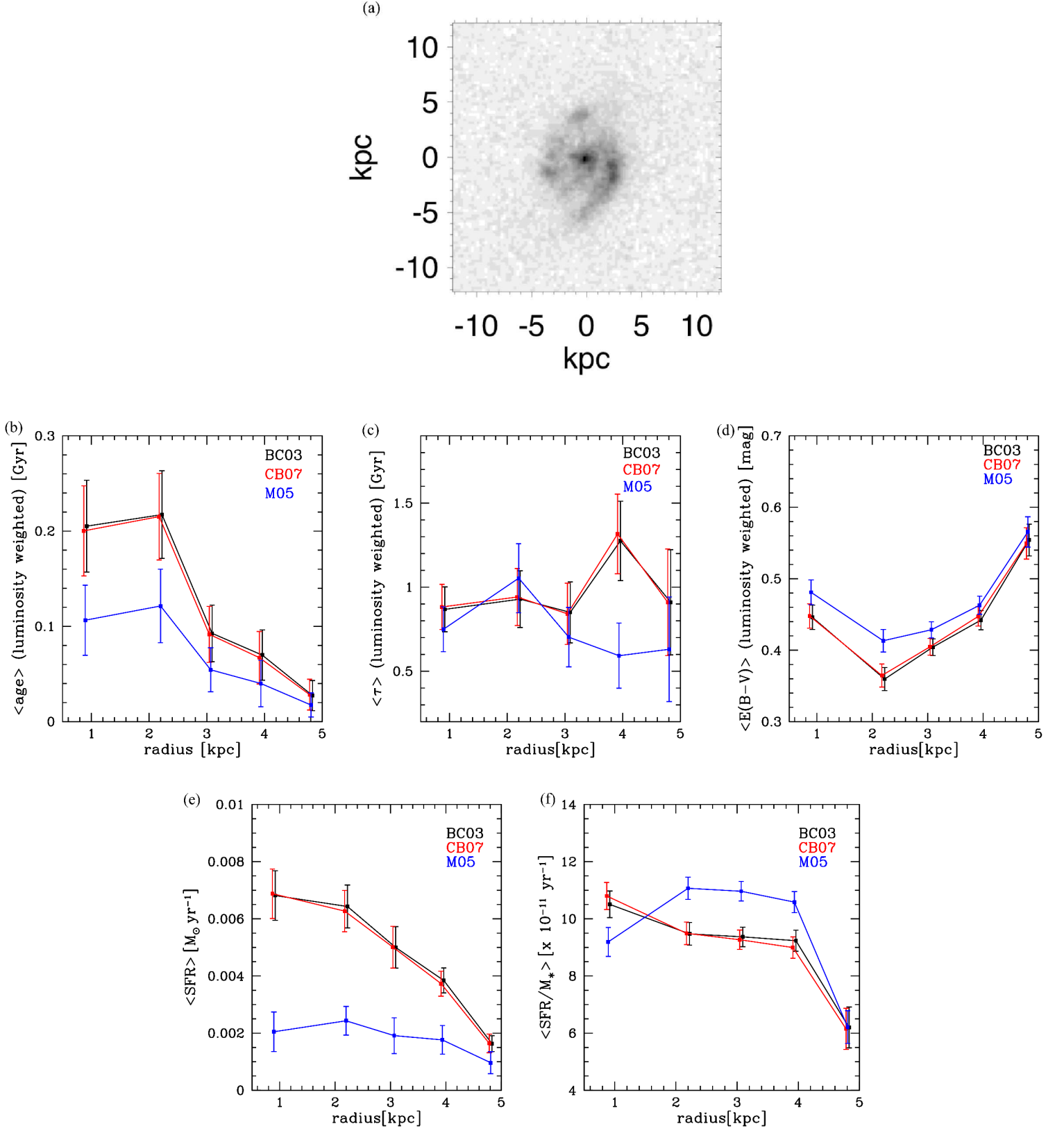
FIG. 15.— The effect of stellar population synthesis model differences on the the radial variation of stellar population quantities in a disk galaxy at $z = 1.1$. (a) The $i775$ image of the galaxy. The following panels show the radial variation of (b) the luminosity-weighted stellar population age (c) the luminosity-weighted SFR e-folding time τ (d) the dust obscuration given in terms of $E(B - V)$ (e) the mean SFR and (f) and the mean specific SFR (sSFR) across the galaxy. The models tested are BC03 (black), CB07 (red) and M05 (in blue). The innermost annulus is larger than the FWHM of the PSF in the $i775$ image ($0.11''$).
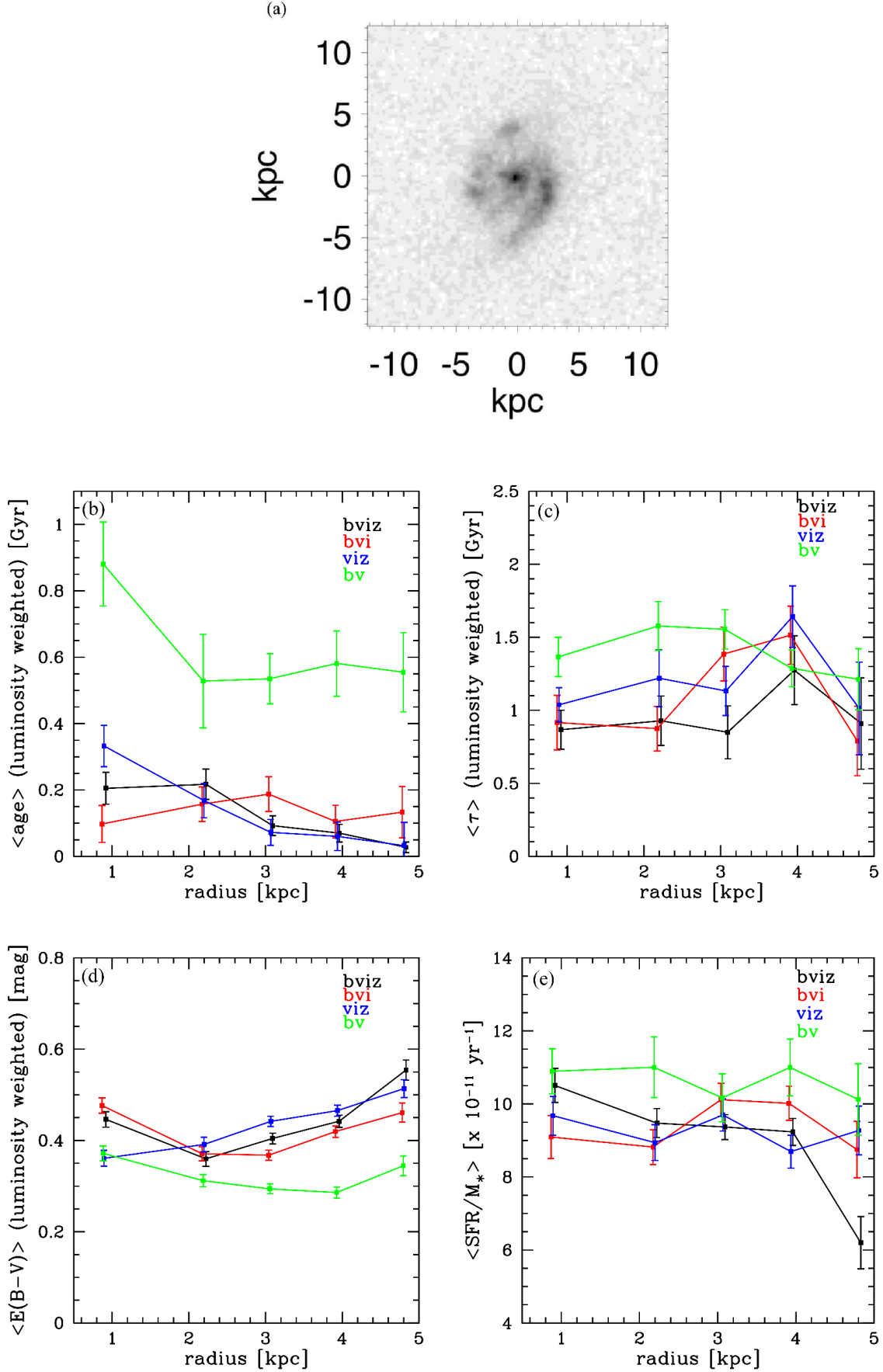
FIG. 16.— The effect of passband differences on the the radial variation of stellar population quantities in a disk galaxy at $z = 1.1$ for a fixed population synthesis model (BC03). (a) The $i775$ image of the galaxy. The following panels show the radial variation of (b) the luminosity-weighted stellar population age (c) the luminosity-weighted SFR e-folding time τ (d) the dust obscuration given in terms of $E(B-V)$ (e) the mean specific SFR (sSFR) across the galaxy. The passbands tested are $bviz$ (black), bvi (red), viz (blue) and bv (green). The innermost annulus is larger than the FWHM of the PSF in the $i775$ image ($0.11''$).
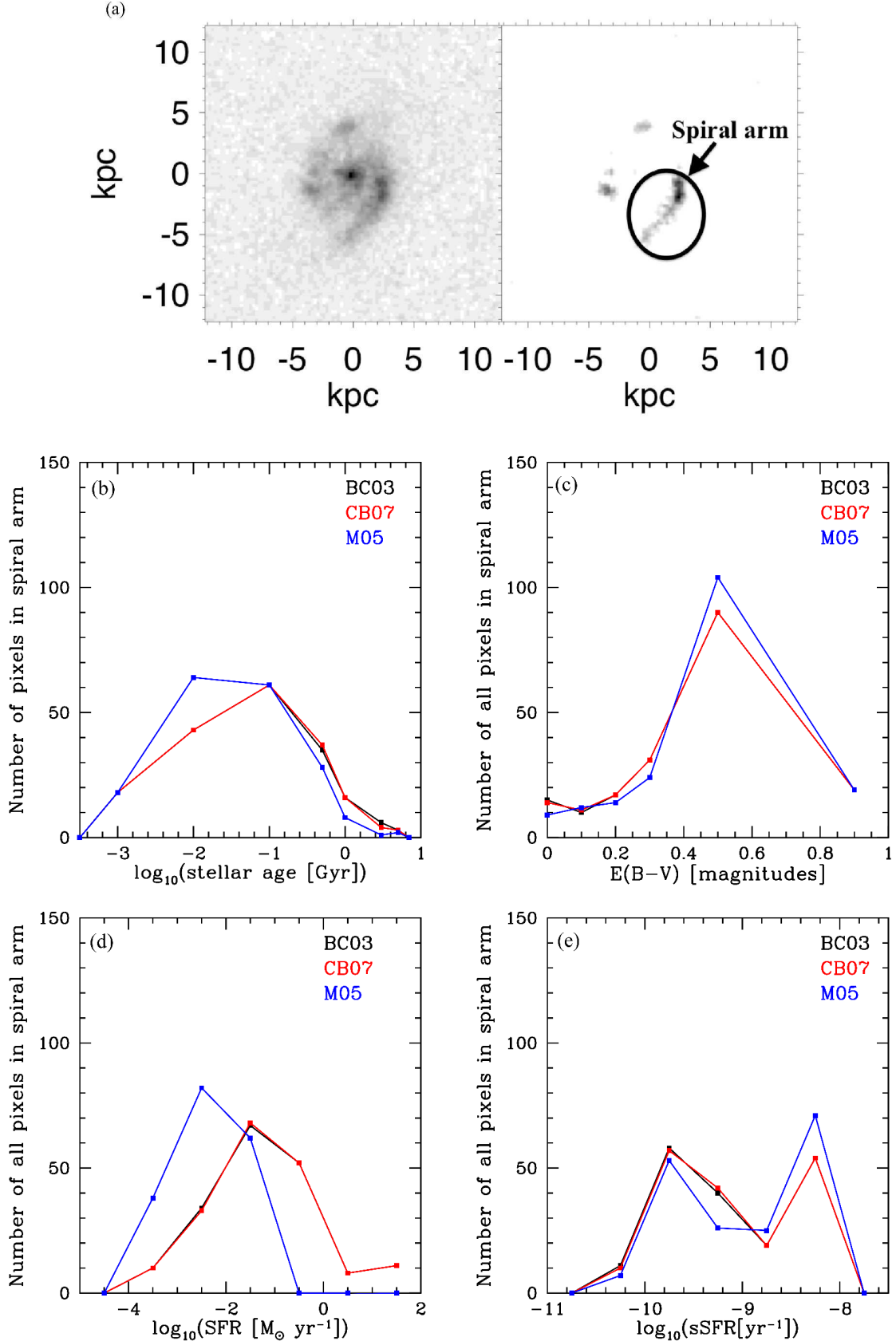
FIG. 17.— Spiral arm structure with pixel-z: the distribution of stellar population properties within a spiral arm. (a) The i775 image of the galaxy (left) and the right spiral arm of the galaxy which has been isolated using GALFIT (right). The remaining panels show the distribution for the pixels within the spiral arm of the following parameters: (b) the stellar population age (c) dust obscuration (d) the SFR and (e) the specific SFR (sSFR). Three population synthesis models are shown in each panel: BC03 (black), CB07 (red) and M05 (blue).
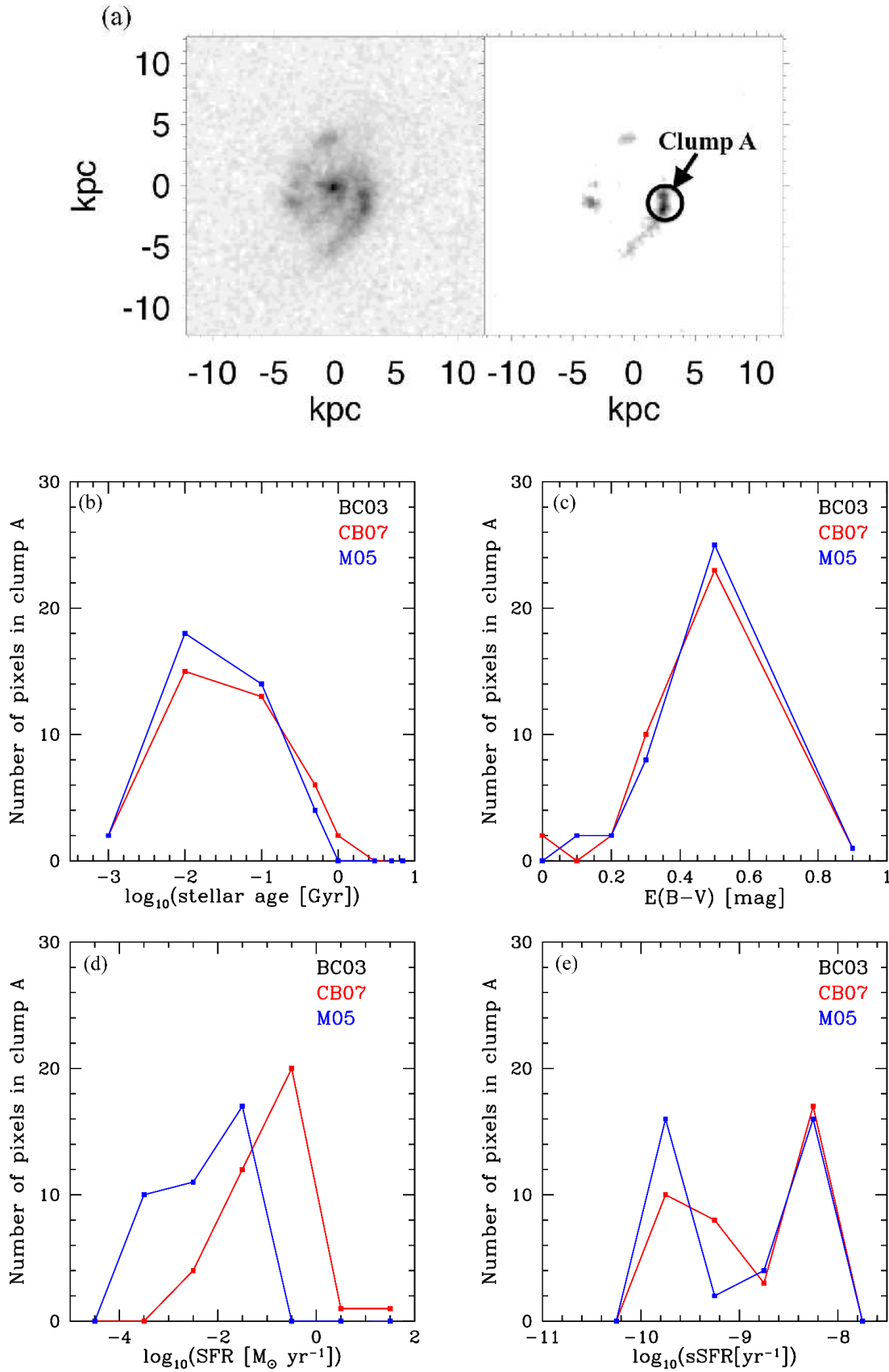
FIG. 18.— Clump structure with pixel-z: the distribution of stellar population properties within clump A of the galaxy. (a) The $i775$ image of the galaxy (left) and clump A which has been isolated using GALFIT (right). The remaining panels show the distribution for the pixels within clump A of the following parameters: (b) the stellar population age (c) dust obscuration (d) the SFR and (e) the specific SFR. Three population synthesis models are shown in each panel: BC03 (black), CB07 (red) and M05 (blue).
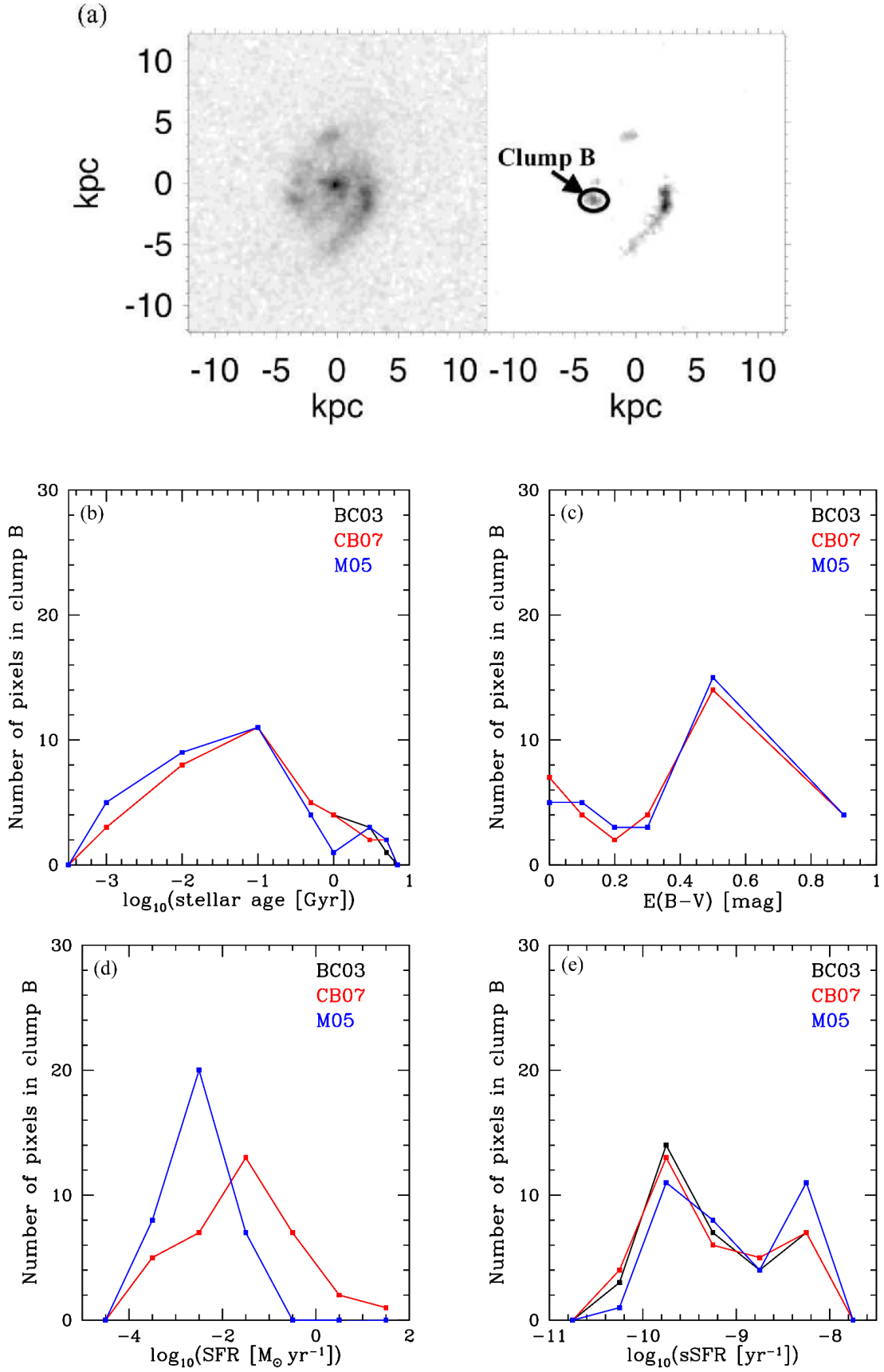
FIG. 19.— Clump structure with pixel-z: The distribution of stellar population properties within clump B of the galaxy. (a) The $i775$ image of the galaxy (left) and clump B which has been isolated using GALFIT (right). The remaining panels show the distribution for the pixels within clump B of the following parameters: (b) the stellar population age (c) dust obscuration (d) the SFR and (e) the specific SFR. Three population synthesis models are shown in each panel: BC03 (black), CB07 (red) and M05 (blue).
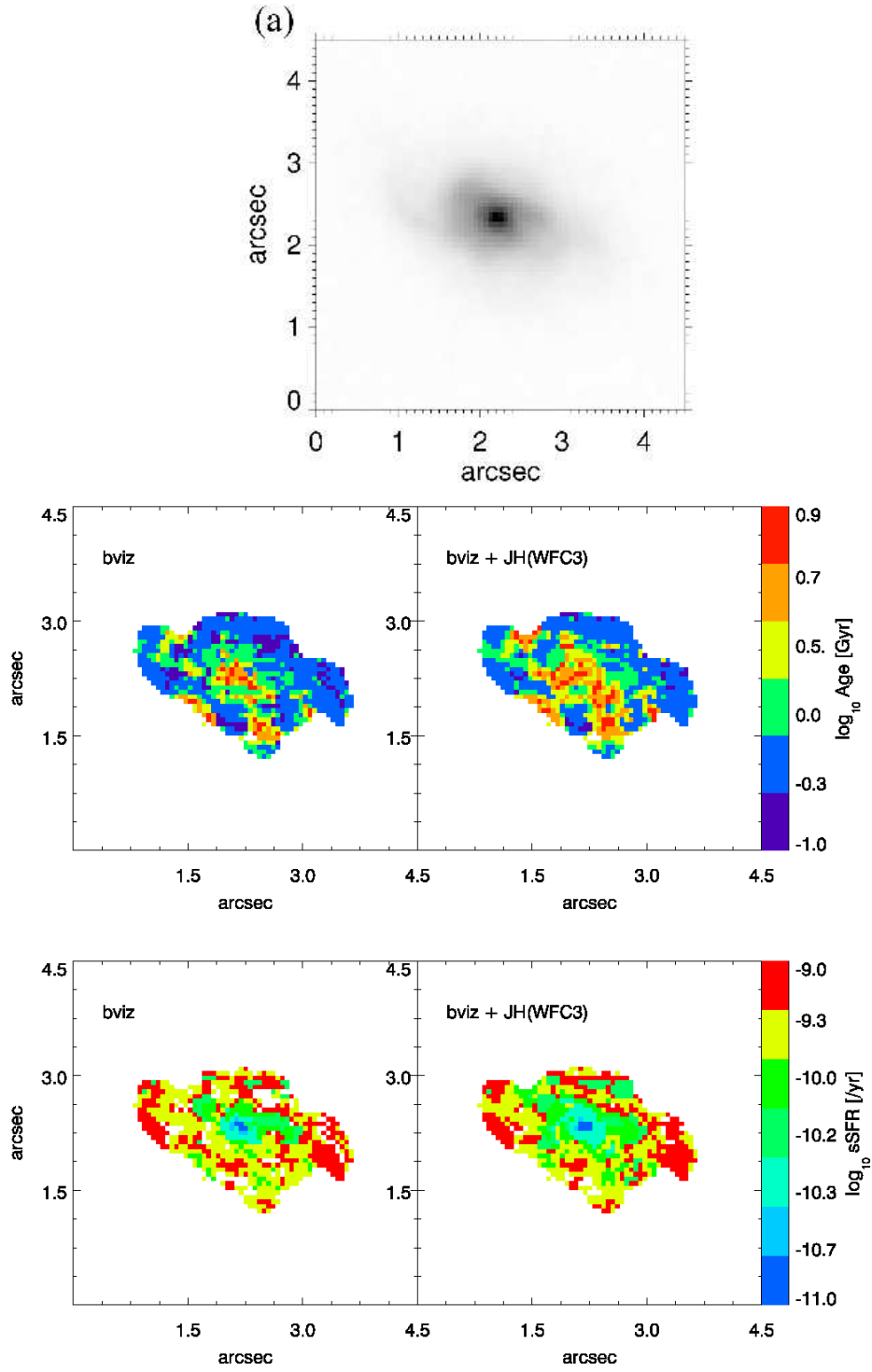
Welikala et al.

FIG. 20.— Effect of adding WFC3 J and H band images from the CANDELS survey on the derived pixel-z parameters using the Maraston 05 stellar population synthesis models (a) H band image of a galaxy at $z = 0.6$ (b) Stellar population age map of the galaxy obtained using the $bviz$ passbands (left) and the $bvizJH$ bands (right) (c) Specific SFR (sSFR) map of the galaxy obtained using the $bviz$ passbands (left) and the $bvizJH$ bands (right).
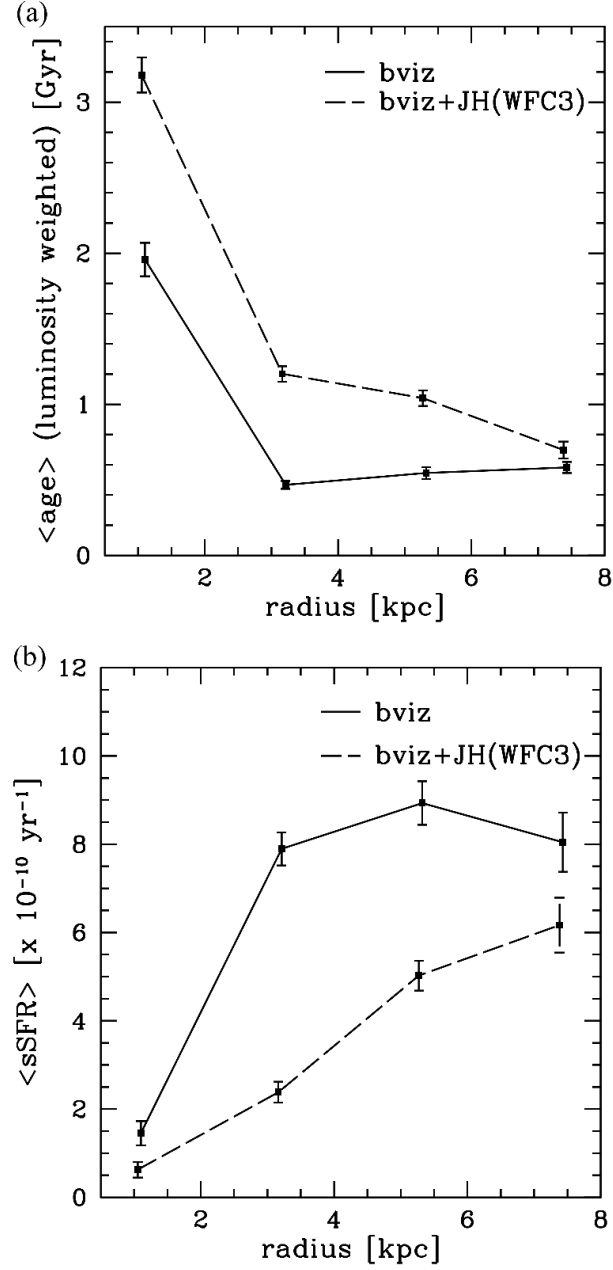
Fig. 21.— Effect of adding WFC3 *J* and *H* band images from the CANDELS survey on the radial variation of the pixel-*z* parameters across the galaxy in Figure 20. The Maraston 05 stellar population synthesis model was used. (a) Radial variation of the stellar population age using the *bviz* passbands (solid line) and the *bvizJH* bands (dashed line) (b) Radial variation of the specific SFR (sSFR) using the *bviz* passbands (solid line) and the *bvizJH* bands (dashed line).